Spectra of p, d, and t from relativistic nuclear collisions

A. Sandoval, H. H. Gutbrod, W. G. Meyer,* R. Stock, and Ch. Lukner†
Gesellschaft für Schwerionenforschung, Darmstadt, West Germany

A. M. Poskanzer, J. Gosset,‡ J.-C. Jourdain,§ C. H. King,‖ G. King,¶ Nguyen Van Sen,** G. D. Westfall, and K. L. Wolf††
Lawrence Berkeley Laboratory, Berkeley, California 94720
(Received 17 September 1979)

Inclusive energy spectra of protons, deuterons, and tritons were measured with a telescope of silicon and germanium detectors with a detection range for proton energies up to 200 MeV. Fifteen sets of data were taken using projectiles ranging from protons to ^{40}Ar on targets from ^{27}Al to ^{238}U at bombarding energies from 240 MeV/nucleon to 2.1 GeV/nucleon. Particular attention was paid to the absolute normalization of the cross sections. For three previously reported reactions, He fragment cross sections have been corrected and are presented. To facilitate a comparison with theory the sum of nucleonic charges emitted as protons plus composite particles was estimated and is presented as a function of fragment energy per nucleon in the interval from 15 to 200 MeV/nucleon. For low-energy fragments at forward angles the protons account for only 25% of the nucleonic charges. The equal mass ^{40}Ar plus Ca systems were examined in the center of mass. Here at 0.4 GeV/nucleon ^{40}Ar plus Ca the proton spectra appear to be nearly isotropic in the center of mass over the region measured. Comparisons of some data with firestreak, cascade, and fluid dynamics models indicate a failure of the first and a fair agreement with the latter two. In addition, associated fast charged particle multiplicities (where the particles had energies larger than 25 MeV/nucleon) and azimuthal correlations were measured with an 80 counter array of plastic scintillators. It was found that the associated multiplicities were a smooth function of the total kinetic energy of the projectile.

[NUCLEAR REACTIONS U(^{20}Ne,X), E/A=240 MeV/nucleon; U(^{40}Ar,X), Ca(^{40}Ar,X), U(^{20}Ne,X), Au(^{20}Ne,X), Ag(^{20}Ne,X), Al(^{20}Ne,X), U(^{4}He,X), Al(^{4}He,X), E/A=390 MeV/nucleon; U(^{40}Ar,X), Ca(^{40}Ar,X), U(^{20}Ne,X), U(^{4}He,X), U(p,X), E/A=1.04 GeV/nucleon; U(^{20}Ne,X), E/A=2.1 GeV/nucleon; measured $\sigma(E,\theta)$, $X=p, d, t$.]

I. INTRODUCTION

In our previous experiment[1] to measure protons and light nuclei produced in central collisions of relativistic heavy ions we mainly studied the systems ^{20}Ne on U at 250 MeV/nucleon, and ^{20}Ne and ^{4}He on U at 400 MeV/nucleon. Energy spectra for p, d, t, ^{3}He, and ^{4}He were obtained at angles between 25° and 150° in the energy range from 30 to about 100 MeV/nucleon. The detector telescope consisted of a 2-mm-thick silicon ΔE detector followed by a 10-cm-thick plastic scintillator E detector. In order to measure the associated multiplicity of charged particles a tag counter array consisting of 15 plastic scintillator paddles was placed outside the scattering chamber. The scintillators were triggered by particles from the target with at least 50 MeV nucleon of energy and covered an area of only 8% of 4π sr.

These first measurements, giving an overview of the main products of relativistic heavy-ion reactions, were of considerable interest. We generated the nuclear fireball model[2] to describe the proton data, and applied a coalescence model[3] to the light composite nuclei. Subsequently, chemical equilibrium in the fireball was proposed to describe the production of pions[4] and light composite nuclei.[5-7] Meanwhile, the fireball model was generalized to the firestreak[8] and then combined with the chemical equilibrium concept to provide predictions for all light particles in a self-consistent thermal model.[9] The fireball model has also been used to predict pion multiplicity distributions,[10] and a two fireball model, as originally proposed,[2] has been resurrected.[11] The fireball model has been extended to the higher energy domain,[12] and the addition of compression and expansion effects are beginning to be incorporated.[13-15] An examination of the statistical basis of the model has also been done.[16] A related model which has been proposed is the effective target-effective projectile model.[17]

Our data, particularly for the case of 250 MeV/nucleon ^{20}Ne ions on a uranium target, have also been compared with many other model calculations. Several reviews of these comparisons have been presented.[18-20] The models which have been used include the intranuclear cascade,[18,21-23] hard spheres,[18] rows on rows,[24,25] fluid dynamics,[26] two-fluid dynamics,[27] fireball,[1,2] firestreak,[9] compressed fireball,[14] average prototype event,[28] and single scattering.[29,30] Also of interest on this subject are another recent review article[31] and

two conference proceedings.[32,33]

Because of this widespread interest in our early data[1] taken with a silicon and plastic scintillator telescope and with a small tag counter array, it was clear that improved and more extensive measurements were necessary. A telescope was built in which the E detector was 7 cm of intrinsic germanium, rather than plastic scintillator. The tag counter array was expanded from 15 to 80 plastic scintillators, covering two-thirds of the forward hemisphere, and capable of measuring multiplicity pattern as a function of both polar and azimuthal angles. A thinner-walled scattering chamber was built which allowed charged particles to reach the tag counter array with energies as low as 25 MeV/nucleon, and pions as low as 10 MeV. A technique to measure positive pions was added. A large set of data was taken using projectiles from protons to ^{40}Ar on targets from ^{27}Al to ^{238}U at bombarding energies from 240 MeV/nucleon to 2.1 GeV/nucleon. In addition, for cross section normalization, a completely independent and more basic procedure was instituted. In the course of this work it was found that the absolute normalization of some of the old data was high by a factor of 2.5 to 3. Unfortunately, this has caused considerable confusion, for which we apologize, in the many comparisons of the old data to the model calculations.

In this paper we will be presenting the experimental techniques and the single-particle inclusive spectra for p, d, and t. The matrix of target-projectile combinations which we have studied is shown in Table I. The π^+ results for one case have already been presented,[34] and the rest of the π^+ data will be appearing in a subsequent paper, as well as the multiplicity-selected p, d, and t data.

II. EXPERIMENTAL TECHNIQUES

The scattering chamber is shown in Fig. 1. It consists of a one meter diameter sphere of aluminum made with 3-mm-thick walls. The beams used and their energies are listed in Table I. The energies have been corrected for degradation in the windows and air gap upstream of the scattering chamber. The beam spot size was about 1 cm high by 1.5 cm wide. The targets were 2.5 cm high by 5 cm wide with thicknesses which are also listed in Table I. The targets were placed at 45° with respect to the beam. The Ca targets was always protected in an argon atmosphere until the chamber was evacuated. All the targets were supported on their edges with 1 mg/cm^2 Mylar film in a plastic frame. Blank measurements were made when necessary with the Mylar and frame in place.

A. Detector systems

1. Multiplicity array

The multiplicity array, just outside the scattering chamber, consisted of 80 plastic scintillator paddles as shown in Fig. 1. The paddles were 6.4 mm thick and were arranged in four azimuthal rings covering the laboratory polar angles indicated in Fig. 2. Ring A consisted of 16 paddles, each covering 15° of azimuth. Rings B and C both had 30 paddles, each covering 10° in azimuth. Ring D consisted of four paddles placed at backward angles in the horizontal plane. The fraction of the azimuth covered by each ring is also indicated in Fig. 2. The coverage of the three forward rings was incomplete in order to avoid having paddles shadowed by the flanges of the scattering chamber. Each paddle was connected by a 15-cm light guide to a 5-cm-diam photomultiplier

TABLE I. The combinations of target, projectile, and bombarding energy which were studied. The target thicknesses are indicated in parentheses.

		Targets (mg/cm^2)				
Projectile	Energy (MeV/nucl)	Al (109)	Ca (200)	Ag (185)	Au (196)	U (200)
p	1041					X
^{4}He	399	X				X
	1049					X
^{20}Ne	241					X
	393	X		X	X	X
	1045					X
	2095					X
^{40}Ar	388		X			X
	1042		X			X

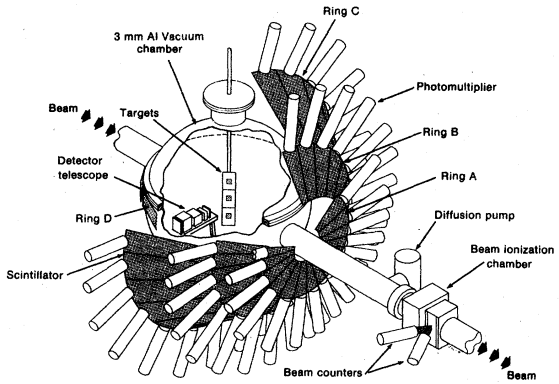

FIG. 1. Schematic diagram of the scattering chamber, telescope, and associated multiplicity array. Also shown are the beam ionization chamber and the beam scintillation counters used for calibration.

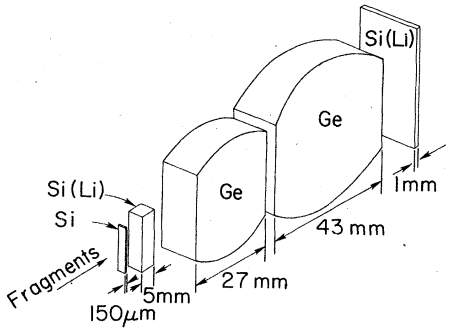

FIG. 3. Schematic diagram of the telescope with the thickness of the detectors indicated. The other dimensions are given in Table II. The germanium detectors were isolated in a liquid nitrogen cryostat, while the silicon detectors were on a refrigerated mount.

tube. A red-light emitting diode (LED type MV50) was attached with a small air gap to the base of each light guide and pulsed at a slow rate during the experiment to monitor gain stability.

2. Telescope

The special ΔE-E-E_{rej} detector system shown in Fig. 3 was developed to measure stopped particles up to a proton energy of 200 MeV. The ΔE detectors consisted of a 150 μm Si(P) and a 5-mm Si(Li). The latter was constructed with a guard ring which surrounded the periphery of its active area. The guard ring was employed to improve the edge field of the detector and it also served as an anticoincidence collimator. The dead layer at the back of this detector was measured to be 25 μm using ^{241}Am alpha particles. The rejection detector E_{rej} was a large area Si(Li). All three detectors were cooled to $-30\,^{\circ}$C by an external circulating refrigerated bath.

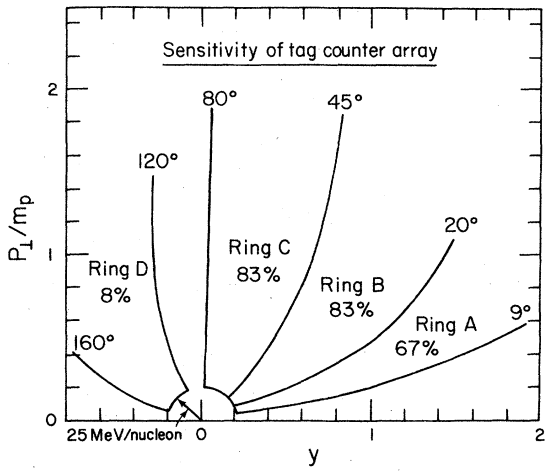

FIG. 2. Sensitivity of the tag counter array shown on a transverse momentum versus rapidity diagram. The lines are drawn at the polar angles which define the edges of the rings. The percentages indicate the percent of the azimuth covered by each ring. The low-energy cutoff for protons and light nuclei due to the thickness of the chamber wall is indicated.

Intrinsic germanium detectors were developed for E counters and were aligned so that the particles entered the crystal perpendicular to their field lines. This arrangement allowed the use of only two individual germanium crystals to obtain an E thickness of 70 mm. Thus, in contrast to normal entry systems which would need about seven counters, the disturbing effects of dead layer in the entrance and exit window of each individual counter were very much reduced. The side entry, however, required sophisticated procedures in the fabrication of the counters (i.e., proper crystal orientation) in order to guarantee a uniform thickness of the dead layer across the width of the counter. The side-entry dead-layer thickness at the entrance of the first germanium detector was made as small as 4 μm, measured by absorption of 60 keV gammas from ^{241}Am. Both counters had a Li-diffused n^+ contact and a $^{11}B^+$ implanted p^+ contact. The dimensions are given in Table II.

The counters required high vacuum and ultraclean environment. A special cryostat was built nearly completely out of aluminum in order to avoid long-lived radioactivity induced by the beam halo. It contained a $\frac{3}{4}$ liter liquid nitrogen reservoir which cooled the counters as well as a molecular sieve acting as a cryopump. The Dewar was constructed with about 15 layers of "super insulation" and had a boil off rate of only 1 liter/20 hours. When the cryostat with detectors was mounted inside the vacuum of the scattering

TABLE II. The detector characteristics.

	Type	Thick (mm)	Width (mm)	Max. height (mm)	Volume (cm^3)	Lower level (MeV)	Upper level (MeV)
Telescope							
$E1$	Si(P)	0.150	3	13		0.25	6
$E2$	Si(Li)	5.0	5	15		1.5	32
$E3$	Ge	27	12.2	39	11.8	10	230
$E4$	Ge	43.5	15.1	51.4	29.5	10	230
$E5$	Si(Li)	1	20	44		0.5	
Monitor							
ΔE	Si(P)	0.120	10	10		5	12
E	Si(P)	0.356	10	10		1	25
E_{rej}	Si(P)	0.360	10	10		0.5	

chamber, the liquid nitrogen was fed through a flexible stainless steel bellows from the outside of the scattering chamber. The experiment was stopped every 10 hours for 10 minutes for the filling procedure. The entrance windows and two side windows used for tests with radioactive sources were made of 0.025 mm Havar whereas the exit window facing towards the E_{rej} counter was made of 0.4 mm aluminum.

3. π^+ identification

The telescope was also used to measure positive pions. When a π^- stops in the germanium detectors it is captured in a nucleus and the resultant nuclear disintegration destroys the kinetic energy information. However, a stopped π^+ undergoes the following decays:

$$\pi \xrightarrow{+26\,\text{ns}} \mu^+ + \nu\,,$$

$$\mu \xrightarrow{+2.2\,\mu\text{s}} e^+ + \nu + \bar{\nu}\,.$$

The π^+ decay is short compared to our amplifier time constants and thus the 4.2 MeV of the μ^+ is added to the pion energy signal. However, the μ^+ is long lived enough so that we may observe a delayed coincidence between the stopped π^+ and the emitted e^+. The positrons have a maximum energy of 53 MeV and a spectral shape given by $2w^2(3-2w)$, where w is the positron energy divided by its maximum energy. This spectral shape is zero at zero energy, peaks at the maximum energy, and has an average of 37 MeV. Thus there is a very good chance of detecting these positrons as they escape from the germanium. By observing this delayed coincidence with a 2.2 μs mean life, in conjunction with the ΔE and E signals, we have been able to sensitively identify the positive pions. This detection method is particularly useful for low-energy pions because it allows, due to its compact geometry, the use of a small flight path between target and detector. Therefore, the corrections for π^+ decaying in flight are much smaller than in magnetic systems.

4. Monitor telescope

A monitor telescope was attached to the inside cover of the scattering chamber at 90° to the beam and 45° above the horizontal plane. Its purpose was to monitor alpha particles from the target between 13 and 30 MeV, which, for a uranium target, encompasses the peak of the evaporation spectrum. The dimensions of the detectors are given in Table II. The telescope was collimated to 8×8 mm and was 22 cm from the target. The monitor telescope served as a check on the beam intensities deduced from the beam monitor ionization chamber described in the next section.

B. Normalization

For the new data presented in this paper it was decided to obtain a new and completely independent method for normalizing the cross sections based on solid angle measurements and counting of particles in the beam. The beam monitor was an ionization chamber which was calibrated by the method to be described, with scintillation counters placed as shown in Fig. 1.

1. Ionization chamber calibration

The parallel plate ionization chamber was filled with argon gas at 800 Torr and contained 11 foils of 0.006-mm Al spaced 3.2 mm apart, with 0.13-mm Al windows. The chamber was operated at +150 V, which was the midpoint of a 200-V plateau. The charge collected from the ionization chamber was integrated for each beam burst on known capacitors by an electrometer.

The first scintillation counter downstream con-

sisted of a 6.4-mm-thick paddle. This was followed by a beam sampling scintillator[35] which consisted of a 6.4-mm-thick Lucite paddle containing scintillation fibers placed in holes drilled parallel to the beam. The fibers were 1 mm in diameter, placed 5.1 mm apart, so that 676 fibers were necessary to cover an area 12.7 cm by 12.7 cm. Both paddles were mounted on RCA 8575 photomultipliers with bases designed for high rates and connected to MECL III discriminators and fast scalers. At low beam rates the ratio of the sampling scintillator to the normal scintillator was determined to be 2.8%, and then the ratio of the ionization chamber to the sampling scintillator was determined at beam rates which varied up to a maximum of 10^8 particles/sec, above which the phototube on the sampling scintillator saturated. The pulse height spectrum of the sampling scintillator contained some tailing below the peak and thus its efficiency was slightly dependent upon the discriminator setting. However, in the final calibration of the ionization chamber relative to the normal scintillator this factor exactly canceled out.

The results for the calibration of the ionization chamber with two beam energies of Ne and one of Ar are shown in Fig. 4. The abscissa is the theoretical dE/dx of the beam, taken as Z^2 times the dE/dx of a proton with the same velocity.[36] The straight line through the origin, whose slope was determined to about 6%, was taken as the experimental ionization chamber calibration. One can also estimate the calibration from first principles, knowing the dimensions of the ionization chamber, the size of the integrating capacitor, and the value $\epsilon = 26.4$ eV/ion-pair[37] for Ar gas. The experimental slope is 81% of this calculated slope, which is probably due to the fact that the calculated slope assumes no losses of charge anywhere in the system. It should also be noted that the Ar point does not lie below the line, which would be the case of the ionization chamber suffered from incomplete charge collection at high ionization density.

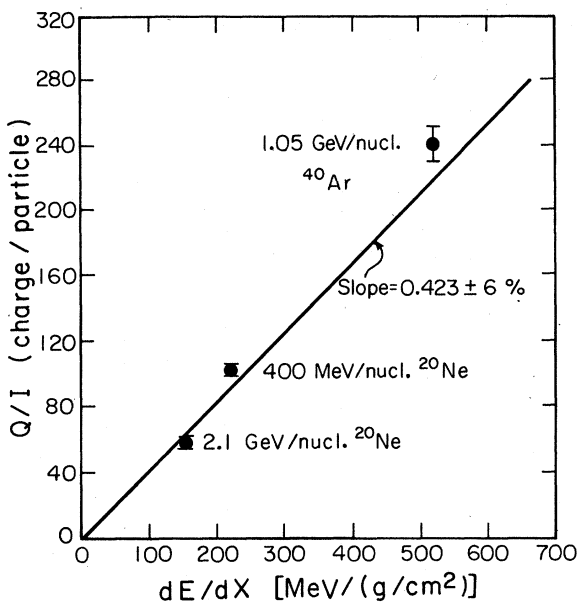

FIG. 4. The ionization chamber calibration curve. The collected charge per incident particle is plotted versus the theoretical rate of energy loss of the particle.

2. *Solid angles*

The solid angle of the telescope was determined from the active area of the detector and the target to detector distance. As described in the electronics section below, either of two coincidence requirements triggered the recording of an event, thus forming "thin" and "thick" telescope events. Detectors $E1$ and $E2$ formed the thin telescope and its solid angle was defined by $E1$. Detectors $E2$, $E3$, and $E4$ formed the thick telescope, with $E2$ defining the solid angle. The active areas of $E1$ and $E2$ were determined by means of a calibrated ^{241}Am alpha particle source. From these measurements the solid angles were determined to be 0.55 msr ± 2% for $E1$ and 0.85 msr ± 4% for $E2$, yielding a solid angle ratio (thick/thin) of 1.54 ± 4.5%. Since $E2$ was 5 mm thick with a guard ring, the method of determining the active area as described above may have an inherent error due to the short range of the alpha particles used. In order to avoid such an error, the solid angle ratio was also determined from the p, d, and t data themselves as a function of energy. The mean solid angle ratio obtained was 1.54 with an average deviation of 3.3% for each measurement. This agrees with the ratio determined by the alpha source.

3. *Old data*

It is believed that the normalization of the new data is accurate to 20%. However, when comparing with the old data,[1] it was found that the old data for protons from 250 and 400 MeV/nucleon ^{20}Ne on U were high by factors of about 2.4, and about 30% more at the most forward angle. The old data had been normalized by the following very indirect procedure. They were first normalized to lower-energy fragment data in the evaporation region by means of a graphical extrapolation, which was necessary because the two sets of data did not overlap in the energy ranges

covered. These data for incident heavy ions were then normalized to data for incident high-energy protons,[38] assuming that the beam monitoring ion chamber response was linear with dE/dx. The data for high-energy protons on a U-target had been normalized by integrating the spectra for the emitted ^{7}Be fragments over both energy and angle and comparing to the radiochemically measured ^{7}Be production cross section. This in turn had been determined in a stacked-foil irradiation relative to the yield of ^{7}Be from an Al target, which had been determined relative to the yield of ^{11}C from a C target. This last activation cross section had been determined by counting protons in a beam. The weakest step in this long chain was probably the graphical extrapolation mentioned first. The additional discrepancy at the most forward angle is now known to be due to improper background subtraction caused by not measuring the blank using the target frame and Mylar support. Such measurements have been done with the new data, and, in addition, improvements in the beam line have greatly reduced the background at forward angles.

We must emphasize that we have much more confidence in the new data. The old p, d, and t data are superseded by the present data and the old ^{3,4}He data have been corrected and will be presented below. Our previous paper[1] also presented data for ^{4}He to ^{10}Be fragments in the low-energy region of 0.5–8 MeV/nucleon and Li to O fragments at higher energies. We believe these data to be correct because they did not depend upon the graphical extrapolation.

C. Electronics

A block diagram of the electronics is shown in Fig. 5. Fast (40 ns) coincidences were required between $E2$ and $E1$ (called thin) or between $E2$ and one of the germaniums (called thick). The timing was set by the time of the $E2$ pulse. Pile-up rejectors were used on $E1$–$E4$. On the slow side, single channel analyzers were used with the settings shown in Table II. The constant fraction discriminators were always set below these lower levels. A slow coincidence of either the thin or thick types generated the master logic signal.

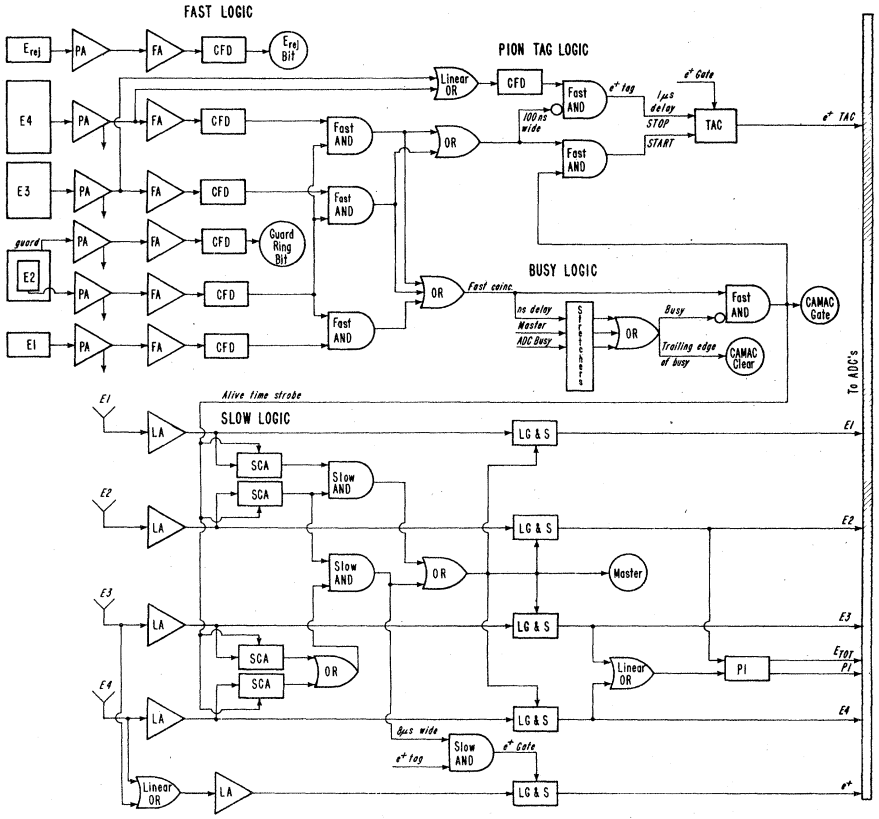

FIG. 5. An electronic block diagram. PA=pre-amplifier, FA=fast amplifier, LA=linear amplifier, CFD=constant fraction discriminator, SCA=single channel analyzer, LG and S=linear gate and stretcher, TAC=time-to-amplitude converter, PI=analog particle identifier, and ADC=analog-to-digital converter.

The logic of the monitor telescope was similar and the linear signals from it were mixed with those from the germanium telescope before going to those of the analog-to-digital converter (ADC). Bits were set in the computer by means of a CAMAC interface for the guard ring and E_{rej} detectors, the pile-up rejectors, the thin and thick coincidences, the monitor telescope, and the pulser triggers.

The busy signal was generated by combining the fast coincidence, master, and ADC busy pulses, first stretching the fast coincidence so that it would overlap the beginning of the master, and stretching the master so that it would overlap the beginning of the ADC busy. However, the fast coincidence was delayed a few nanoseconds so that the final busy signal would not inhibit the fast coincidence which generated it. This fast coincidence acted as the CAMAC gate. The CAMAC clear was generated on the trailing edge of the busy.

The pion tag logic was used to record the time between the stopped positive pion and the delayed positron emission. The germanium signals were combined and sent to a separate constant fraction discriminator set at 1 MeV. The output was inhibited for the first 100 ns after a thick coincidence, but then could produce an e^+ tag signal. This was delayed by 1 μs and used to stop the e^+ time-to-amplitude converter, which recorded delayed coincidences in the range of 1–8 μs.

For the scintillation counter array, the signals from the 80 photomultipliers were sent to CAMAC discriminators. The discriminators were set at 100 mV and the tube high voltages were adjusted to put the pulses from the 1 MeV electrons of a ^{207}Bi source at this voltage. The CAMAC gate, which was generated by the telescope fast coincidence, was 25 ns wide.

Electronic pulsers were used to feed signals to all the detectors. The pulser trigger was derived from the E_{rej} detector of the monitor telescope. It was scaled down by an appropriate factor and delayed 4 μs before triggering the pulsers. Because the pulsers were triggered at a rate proportional to the beam intensity they could be used to determine the system dead time. For the Si and Ge detectors the pulser coupling capacitors were adjusted to give an energy calibration based on ϵ values of 3.61 eV/ion-pair for Si and 2.96 eV/ion-pair for Ge. The light-emitting diodes on the scintillation counters were fired by an 80-output avalanche pulser triggered in the same way. However, this trigger was turned off every other beam burst by a relay in order to measure the accidental rate (trigger off) and dead time (trigger on) in the scintillator array.

D. Data reduction

1. Differential cross sections

The raw data were stored event by event on magnetic tape, each event consisting of the 8 pulse heights indicated in Fig. 5, the 80 bits of the tag array, and 16 logic bits. The events were sorted according to the type of particle (π, p, d, t) by placing tight polygonal windows defined by 10 points in the plot of the energies in each pair of contiguous detectors which the particle traversed. In addition a more generous window was placed in the $E2$–E_{tot} plane to suppress the contamination of punch through heavy particles.

For particles stopping in $E2$ the defining solid angle was that of $E1$ and the $E2$ guard ring bit was not used. For particles stopping in $E3$ or $E4$ the $E2$ guard ring bit was used in an anticoincidence mode to better define the $E2$ solid angle. The measured total energy of the particle was corrected for the energy loss in half the target thickness, taking an average angle of 10° with respect to the normal to the target. Corrections were also made for the following inactive material, if the particle traversed it: 25 μm dead layer at the back of $E2$, 25 μm Havar window at the entrance of the germanium cryostat, and 380 μm dead layer between the two germaniums. For each run and type of particle a new file of event by event data was created consisting of the particle's energy and the bits and multiplicities of the triggered paddles in the four rings of the tag array. Double differential cross sections with or without multiplicity gating were constructed from energy histograms of these data.

2. Correction factors

To these normalized histograms, corrections were applied for the loss of particles due to reactions while stopping and for scattering out from the detectors.

The fraction of reaction loss for protons in the germanium counters was taken from the literature.[39,40] For deuterons and tritons there are no experimental data for the reaction probability of the relevant energies. Thus, an integration was done using range energy tables and reaction cross sections calculated with the equations

$$\sigma_R(E) = \pi R^2[1 - Z_1 Z_2 e^2/(ER)],$$

$$R = 1.43(A_1^{1/3} + A_2^{1/3})\ \text{fm}.$$

Above 30 MeV for deuterons and 50 MeV for tritons, constant values for σ_R were used equal to the values calculated at these energies. The germanium detectors were subdivided in slices with n_i atoms/cm^2 in slice i. For a given particle en-

ergy E, the mean energy in slice i, E_i was determined from range-energy tables. The efficiency, defined as one minus the fraction lost, was then given by

$$\exp\left[-\sum_i n_i \sigma_R(E_i)\right].$$

Estimated errors in the reaction-loss correction are 10% for protons,[39] and 20% for deuterons and tritons. In Fig. 6(a) is shown the correction used for the reaction loss of protons in the detector.

The scattering-out correction for protons was estimated with a Monte Carlo calculation using the program ANGLE.[41] The irregular shape of each of the germanium counters was approximated by three rectangular slabs which conserved the volume of the detector. A scattered-out particle is defined as one leaving the detector with enough energy so as to be thrown out of the polygonal window used for particle identification. The curve for the efficiency, defined as one minus the fraction of scattered-out protons, is shown in Fig. 6(a). The program ANGLE also calculated the maximum fraction scattered out for deuterons to be 8.4% at 250 MeV, and for tritons to be 4.6% at 300 MeV. The scattering-out correction for these particles was taken from the proton curve as a function of range, normalized to these maximum values. Figure 6(b) shows the efficiencies used for all three particles.

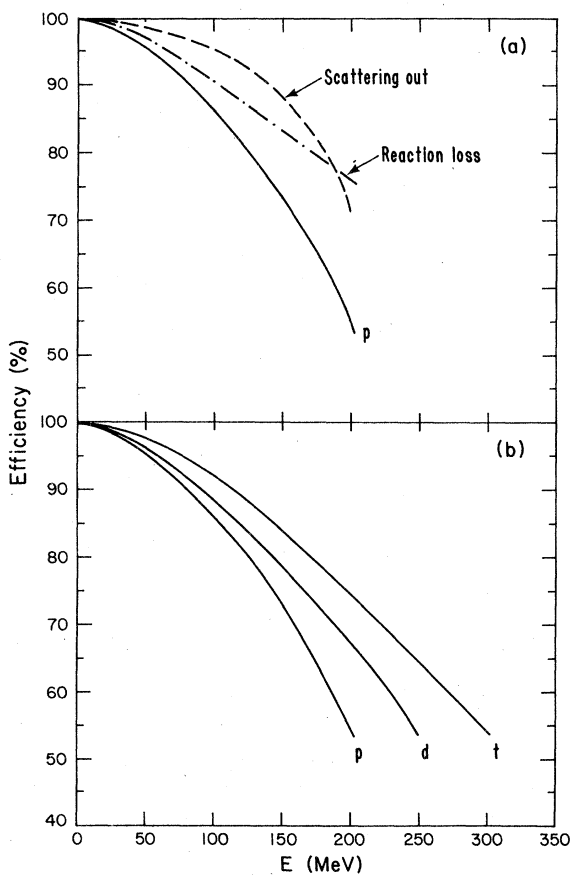

FIG. 6. (a) The efficiency of the telescope for protons due to reaction loss, scattering out, and the combination of both. (b) The efficiencies used for protons, deuterons, and tritons.

In addition the dead layers caused a drop in yield at the energy corresponding to particles stopping in the dead layer, and a pile-up of yield just below this energy. For the dead layer between $E3$ and $E4$ this feature in the data was smoothed out while conserving yield by a three point interpolation. For the dead layer between $E2$ and $E3$ a simple logarithmic interpolation was used.

3. *Summed nucleonic charges*

The light composite particles (d, t, ^{3}He, and ^{4}He) have considerable yields compared to protons and are not included in any theoretical predictions so far, except for the thermodynamic model.[9] All other models, such as hydrodynamic or cascade models, calculate yields without taking into account the coalescence of nucleons into composite particles. Therefore we have attempted to sum the nucleonic charges emitted at each angle and velocity with the equation

$$\sum_i z_i d^2\sigma_i \Big/ [d(E/A)d\Omega].$$

For the purpose of this summing we extrapolated the d and t data out to an energy/nucleon corresponding to the maximum proton energy. This extrapolation was done logarithmically, using the data between 40% and 95% of the maximum energy measured. An arbitrary error of ± 40% was assigned to the extrapolated data for the purpose of estimating its contribution to the error on the summed charges. In a few cases the statistical accuracy of the data upon which the extrapolation was based was poor. For these cases (393 MeV/nucl. ^{20}Ne + Al → t, 1042 MeV/nucl. ^{40}Ar + Ca → t, 1045 MeV/nucl. ^{20}Ne + U → t, 1041 MeV/nucl. p + U → d, t, 2095 MeV/nucl. ^{20}Ne + U → t) the extrapolations should not be trusted. However, their maximum contribution to the summed charges was only 15%. Also, although deuteron and triton data were measured down to energies per nucleon lower than the protons, and were sometimes used in making the extrapolations, they are not presented in the data tables below the lowest proton energy.

The isotopes ^{3}He and ^{4}He were not measured in this experiment. However, in order to estimate

their contribution to the summed charges, our previous data[1] for the He isotopes from 250, 400, and 2100 MeV/nucleon ^{20}Ne plus U have been corrected and renormalized. Multiple scattering corrections for the old Si-plastic telescope were done, using the program ANGLE.[41] The fractions scattered out were 16% for ^{3}He and 19% for ^{4}He at their maximum energies of 100 MeV/nucleon. The reaction-loss corrections were calculated as described above and amounted to only 2% and 3% for ^{3}He and ^{4}He at their maximum energies. The old data were normalized to the new data by means of the triton spectra which were measured in both experiments. However, the He data were not measured at 20° at 250 and 400 MeV/nucleon, nor below a fragment energy of 30 MeV/nucleon. The data were extended down to 15 MeV/nucleon by a logarithmic extrapolation.

4. *Multiplicity from single-particle inclusive data*

Another interesting quantity which can be obtained from our telescope data is $\langle M\rangle_s$, the average multiplicity of charged particles per reaction in the region S of momentum space. This quantity is obtained from the measured single-particle inclusive cross section $d^3\sigma_1/dp^3$ by the relation

$$\langle M\rangle_s = \frac{1}{\sigma_R}\int_s \frac{d^3\sigma_1}{dp^3}\,dp^3 .$$

If the $E_{\rm rej}$ anticoincidence restriction is lifted in the data processing, the detector telescope can be used as a counter for all charged particles which reach or pass through $E2$. This corresponds to a lower-energy threshold of approximately 30 MeV/nucleon. For the angular dependence of the cross section it is necessary to interpolate between and extrapolate beyond the angles of our measurements. Although extrapolation of our measurements into the kinematic region beyond 150° laboratory angle is probably reliable, the preponderance of charged particles at forward angles makes extrapolation to angles less than 10° quite uncertain. This means that the region S within which we can determine $\langle M\rangle_s$ is effectively $E>30$ MeV/nucleon and $\theta_{\rm lab}>10°$.

5. *Associated multiplicities*

The multiplicity array allows us to obtain measurements of the number of charged particles associated with events producing low-energy light fragments (π, p, d, t) which are detected in the telescope at angles between 20° and 150° with respect to the beam direction. For several reasons, however, we do not obtain a direct measurement of the total associated charge-particle multiplicity: (1) The 3-mm-thick aluminum walls of the vacuum chamber produce a lower-energy threshold for the multiplicity array of approximately 25 MeV/nucleon ($E_\pi>10$ MeV, $E_p>25$ MeV, $E_d>34$ MeV, $E_t>40$ MeV, $E_{^3\rm He}>88$ MeV, $E_{^4\rm He}>100$ MeV); (2) the multiplicity array does not cover the full 4π solid angle surrounding the target; (3) it is not possible to determine the simultaneous passage of more than one particle through a given scintillator ("coincidence summing"); and (4) the photomultipliers are subject to dead time and accidental firing. The first three of these effects, of course, tend to reduce the observed multiplicity compared to the real multiplicity.

As described earlier, the accidental rate and dead time in the multiplicity array were determined empirically using light-emitting diodes (LED's) fired in alternate beam bursts by an 80-output avalanche pulser. The relation between the probability that j scintillators have true events, R_j, and the probability that i coincidences are observed, K_i, is given by

$$K_i = \sum_{j=0}^{N} C_{ij}R_j , \tag{1}$$

with

$$C_{ij} = \sum_{k=0}^{i} p^k(1-p)^{N-j-k}q^{j-i+k} \times (1-q)^{i-k}\binom{N-j}{k}\binom{j}{j-i+k},$$

where p and q are the accidental and dead time probabilities, respectively, which are assumed to be the same for all scintillators. For beam bursts in which the LED's are triggered, $R_N=1$ and $R_{i\neq N}=0$ for those events tagged as being LED events.

Thus,

$$q = \frac{K_{N-1}}{(NK_N + K_{N-1})} .$$

Similarly, for beam bursts when the LED's are off, $R_0=1$ and $R_{i\neq 0}=0$. Thus,

$$p = \frac{K_1}{(NK_0 + K_1)} .$$

Once p and q are determined in this manner, expression (1) can be inverted for the non-LED events to obtain the true j-fold coincidence rates R_j.

The effect of the coincidence summing has been considered in several recent papers concerned with γ-ray multiplicity measurements.[42-46] If one assumes that each detector has the same efficiency Ω, and that the emission of particles is uncorrelated and isotropic, it can be shown[42-44] that the probability that m particles are detected

in N detectors when M are emitted is

$$Q_{Nm}^{M}=\binom{N}{m}\sum_{j=0}^{M}\binom{M}{j}\Omega^{j}(1-N\Omega)^{M-j}m!\,\$_{j}^{(m)},$$

where $\$_{j}^{(m)}$ are Stirling numbers of the second kind.[47] Of course, in relativistic heavy-ion collisions, events of various multiplicities M can result. If the probability for having an event of multiplicity M is P_M, then the observed m-fold coincidence rate in N detectors of equal efficiency Ω is

$$R_m=\sum_{M=0}P_M Q_{Nm}^{M}$$

$$=\sum_{j=0}A_{mj}(N)\frac{\Omega^{j}}{j!}\mathfrak{M}_j, \tag{2}$$

where

$$A_{mj}(N)=(-1)^{N+m+j}\binom{N}{m}\sum_{x=1}^{N}(-1)^{x}\binom{m}{N-x}x^{j}$$

and

$$\mathfrak{M}_j=\sum_{M}P_M\binom{M}{j}j!\,.$$

The quantities $\mathfrak{M}_j$ are sometimes referred to as the "pseudo-moments" of the multiplicity distribution P_M. Thus, although the existence of coincidence summing and the missing solid angle prevent us from exactly measuring the multiplicity distribution, the inversion of Eq. (2) allows us to obtain, in principle, pseudo-moments of this distribution from the observed m-fold coincidence rates R_m. A particularly convenient means of performing this inversion is to construct the quantities[42-44]

$$B_m=\sum_{k=m}^{N}\binom{k}{m}R_k\Big/\binom{N}{m}. \tag{3}$$

Then it can be shown that

$$B_m=\sum_{j=0}^{M}(-1)^{j+m}\frac{m!}{j!}\Omega^{j}\$_{j}^{(m)}\mathfrak{M}_j.$$

But then, by the properties of Stirling numbers,[47]

$$\mathfrak{M}_j=\sum_{m=j}(-1)^{j+m}\frac{S_m^{(j)}}{\Omega^{j}}\frac{j!}{m!}B_m, \tag{4}$$

where the $S_m^{(j)}$ are Stirling numbers of the first kind. In the special case of the first moment (average multiplicity $\langle M\rangle$), this reduces to

$$\langle M\rangle=\frac{1}{\Omega}\sum_{m=1}\frac{B_m}{m}. \tag{4a}$$

It should be noted that two main conditions are required to use these analysis techniques for taking into account the effects of accidental firing, dead time, missing solid angle, and coincidence summing: (1) the particle emission should be uncorrelated and isotropic, and (2) the scintillator efficiencies should be equal. For the present apparatus, neither of these conditions is satisfied for all the scintillators. However, since for all heavy-ion induced reactions considered we have observed no strong azimuthal correlation in particle emission, it is not unreasonable to apply these techniques separately to each azimuthal ring. (The proton-induced reaction which we studied, p+U at 1.05 GeV/nucleon, is an exception, since significant azimuthal correlation functions were observed in this case.) We have therefore applied Eqs. (1), (3), and (4) to each ring separately, with Ω chosen to be the fraction of the ring subtended by each scintillator. The corrections to the average multiplicity due to coincidence summing were typically 5–10%, but were as large as 30% for rings B and C in the worst cases (Ar + U at 1.05 GeV/nucleon and Ne + U at 2.1 GeV/nucleon).

This leaves the problem of combining the results for each ring to obtain information about the total multiplicity distribution. A straightforward solution to this problem is obtained if we assume no correlations between particle emission into different rings. Since this is a rather stringent assumption, particularly combined with the other assumptions which have been made, the significance of higher-order moments obtained by using it is suspect. Hence, we have decided only to attempt to extract the average multiplicities in this way. In the absence of correlations, the cross section for a k-particle event is proportional to the product of k single-particle cross sections. Then if one divides the full momentum space into a set of n segments, with $\langle M\rangle_i$ being the average multiplicity in the ith segment, then

$$\langle M\rangle_i=\langle M\rangle f_i, \tag{5}$$

where

$$f_i=\frac{\int_{s_i}\frac{d\sigma}{d\vec{\mathrm{p}}}\,d\vec{\mathrm{p}}}{\int_{\substack{\text{all}\\ \text{space}}}\frac{d\sigma}{d\vec{\mathrm{p}}}\,d\vec{\mathrm{p}}}.$$

Here $d\sigma/d\vec{\mathrm{p}}$ is the single-particle inclusive cross section and s_i the region of momentum space spanned in segment i. That is, in the absence of correlations the average multiplicity in segment i is equal to the average total multiplicity weighted by the fraction of the total particle flux emitted into segment i. Since $\sum_{i=1}^{n}f_i=1$, this can be rewritten

$$\sum_{i=1}^{n}\langle M\rangle_i=\langle M\rangle. \tag{6}$$

Or if, as in our case, the segments correspond to

different regions of solid angle

$$\sum_{i=1}^{n} \frac{\langle M\rangle_i}{\Delta\Omega_i}\Delta\Omega_i = \langle M\rangle ,$$

and in the limit $\Delta\Omega_i \to 0$,

$$\int \frac{d\langle M\rangle}{d\Omega} d\Omega = \langle M\rangle . \tag{6a}$$

Two further approximations are required in using Eq. (6). Since the azimuthal rings of our apparatus do not cover the full space surrounding the target, we are forced to estimate the average multiplicity in other regions by interpolating between and extrapolating beyond the rings. This was done by assuming that $d\langle M\rangle/d\Omega$ has a logarithmic dependence on $\cos\theta$, the slope and intercept being determined by the two neighboring rings to the region of interest. Because the average multiplicity appears to have a complicated dependence at forward angles, extrapolation into this region is quite uncertain. Thus, we only quote the average multiplicity for $\theta > 9°$ with, of course, $E \gtrsim 25$ MeV/nucleon. The increase in calculated average multiplicity resulting from making a logarithmic extrapolation to 0° is typically 5% or less but for some cases (e.g., Ne+Al at 400 MeV/nucleon or Ar+Ca at 0.4 and 1.05 GeV/nucleon) is as high as 10%. Finally, we have ignored the shadowing of the scintillators due to the apparatus inside the chamber. This appears to be minimal for telescope angles of 90° and beyond. Thus, for the most part we have based our conclusions on data satisfying this condition.

6. *Azimuthal correlations*

Some information concerning two-particle azimuthal correlations can be obtained from the dependence of the coincidence rate in the scintillators as a function of the azimuthal angle ϕ with respect to the plane of the telescope (see Fig. 7).

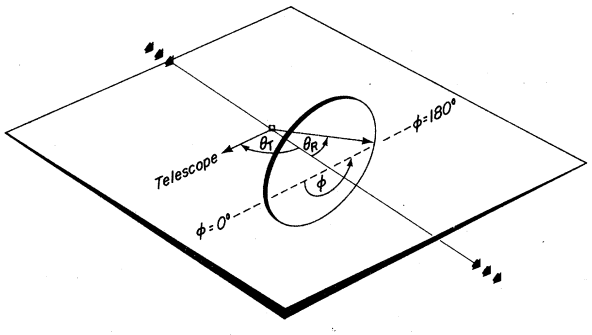

FIG. 7. Diagram of the angles involved in the azimuthal correlation. The plane is defined by the beam and the telescope. The telescope is at the polar angle θ_T and defines the zero of the azimuthal angle ϕ. The polar angles of a scintillator ring are given by θ_R.

The dependence of this correlation on the polar angle of the scintillator ring (θ_R) and that of the telescope (θ_T) can be investigated. A convenient correlation function which can be used[48] is

$$R(\theta_R, \theta_T, \phi) = \sigma \frac{\dfrac{d^2\sigma}{d\Omega_R d\Omega_T}}{\dfrac{d\sigma}{d\Omega_R}\dfrac{d\sigma}{d\Omega_T}} - 1 ,$$

where the uncorrelated contribution $(1/\sigma^2)d\sigma/d\Omega_R d\sigma/d\Omega_T$ to the coincidence rate $(1/\sigma)d^2\sigma/(d\Omega_R d\Omega_T)$ has been removed and then the magnitude is expressed as a fraction of the uncorrelated contribution. We are concerned here more with comparing the results for different projectile-target combinations. Thus, for simplicity (since the singles rate for the scintillators was not measured and can only be deduced approximately from the single-particle inclusive cross sections measured in the telescope) we have assumed that

$$\frac{1}{\sigma}\frac{d\sigma}{d\Omega_R}\frac{d\sigma}{d\Omega_T} \approx \left\langle \frac{d^2\sigma}{d\Omega_R d\Omega_T} \right\rangle ,$$

where the averaging has been taken over ϕ. Hence, we can define an approximate or "quasi-R-function" as

$$R(\theta_R, \theta_T, \phi) = \frac{\dfrac{d^2\sigma}{d\Omega_R d\Omega_T}(\phi)}{\left\langle \dfrac{d^2\sigma}{d\Omega_R d\Omega_T} \right\rangle} - 1 .$$

III. RESULTS

A. Data tables

An example of one page of data is presented in Table III. The laboratory differential cross sections have units of millibarns per MeV per nucleon and per steradian. To obtain cross sections with units of energy one may use the equation

$$\frac{d^2\sigma}{(dEd\Omega)} = \left(\frac{1}{A}\right)\frac{d^2\sigma}{d\left(\dfrac{E}{A}\right)d\Omega} .$$

The invariant cross section may be obtained by

$$\left(\frac{1}{p}\right)\frac{d^2\sigma}{dEd\Omega} .$$

In addition to the statistical errors which are shown, there is an error in the absolute normalization of ± 20% which must be added. The energies listed are the mean energies of the bins. Data preceded by an asterisk are interpolated and those preceded by a dagger are extrapolated, as described above. The last column contains an estimate of the summed nucleonic charges. The contributions of the extrapolated cross sections

TABLE III. Observed, extrapolated, estimated, and summed charges data in mb/[(MeV/A)sr] for 241 MeV/nucl $^{20}Ne + {}^{238}U \rightarrow p, d, t, {}^{3}He, {}^{4}He$ at lab. angle 70 deg. † refers to extrapolated and * to interpolated data. Extrapolated data which is less than 0.1% of the proton yield is omitted. Observed charges include interpolated data but not extrapolated data. Estimated charges include both. The notation $N(x)En$ means $(N \pm x) \times 10^{n}$.

Energy (MeV/A)	p	d	t	^{3}He	^{4}He	Observed charges	Estimated charges
15	2.34(0.04)$E1$	*1.46(0.03)$E1$	*1.19(0.03)$E1$	†3.16(1.28)	†5.64(2.34)	5.00(0.06)$E1$	6.76(0.54)$E1$
21	1.85(0.04)$E1$	*1.36(0.03)$E1$	7.55(0.20)	†2.30(0.93)	†3.23(1.34)	3.96(0.05)$E1$	5.07(0.33)$E1$
27	*1.66(0.03)$E1$	1.20(0.02)$E1$	4.74(0.15)	†1.61(0.42)	†1.85(0.51)	3.34(0.05)$E1$	4.03(0.14)$E1$
33	*1.50(0.03)$E1$	1.03(0.02)$E1$	3.18(0.13)	1.20(0.04)	1.08(0.04)	3.30(0.04)$E1$	3.30(0.04)$E1$
39	*1.35(0.03)$E1$	8.02(0.20)	2.14(0.11)	9.30(0.37)$E-1$	6.13(0.30)$E-1$	2.67(0.04)$E1$	2.67(0.04)$E1$
45	1.21(0.03)$E1$	6.49(0.19)	1.46(0.09)	6.60(0.31)$E-1$	3.87(0.24)$E-1$	2.22(0.03)$E1$	2.22(0.03)$E1$
51	1.16(0.02)$E1$	5.76(0.18)	1.03(0.08)	4.24(0.25)$E-1$	1.94(0.17)$E-1$	1.96(0.03)$E1$	1.96(0.03)$E1$
57	1.13(0.02)$E1$	4.24(0.15)	7.39(0.66)$E-1$	3.44(0.23)$E-1$	1.25(0.14)$E-1$	1.72(0.03)$E1$	1.72(0.03)$E1$
63	1.03(0.02)$E1$	3.42(0.14)	*4.28(0.53)$E-1$	2.60(0.20)$E-1$	7.03(1.06)$E-2$	1.48(0.03)$E1$	1.48(0.03)$E1$
69	1.01(0.02)$E1$	2.93(0.13)	4.17(0.52)$E-1$	1.86(0.17)$E-1$	5.15(0.91)$E-2$	1.39(0.03)$E1$	1.39(0.03)$E1$
75	9.29(0.22)	*2.34(0.12)	†2.93(0.88)$E-1$	1.72(0.17)$E-1$	2.85(0.69)$E-2$	1.20(0.03)$E1$	1.23(0.03)$E1$
81	8.39(0.21)	*1.67(0.10)	†2.10(0.84)$E-1$	9.82(1.26)$E-2$	1.81(0.56)$E-2$	1.03(0.02)$E1$	1.05(0.03)$E1$
87	8.18(0.21)	1.76(0.11)	†1.53(0.62)$E-1$	8.81(1.24)$E-2$	†1.10(0.44)$E-2$	1.01(0.02)$E1$	1.03(0.02)$E1$
93	7.07(0.20)	1.19(0.09)	†1.12(0.45)$E-1$	4.40(0.87)$E-2$		8.34(0.22)	8.45(0.22)
99	7.01(0.20)	1.10(0.09)	†8.14(3.27)$E-2$	3.19(0.76)$E-2$		8.18(0.22)	8.26(0.22)
105	6.30(0.19)	7.89(0.76)$E-1$	†5.93(2.38)$E-2$	†3.31(1.32)$E-2$		7.09(0.20)	7.21(0.21)
111	*5.14(0.18)	7.58(0.76)$E-1$	†4.32(1.73)$E-2$	†2.46(0.98)$E-2$		5.89(0.19)	5.99(0.20)
117	*4.47(0.17)	5.42(0.66)$E-1$	†3.15(1.26)$E-2$	†1.82(0.73)$E-2$		5.01(0.18)	5.08(0.18)
123	4.14(0.16)	4.36(0.61)$E-1$	†2.29(0.92)$E-2$	†1.35(0.54)$E-2$		4.58(0.17)	4.63(0.17)
129	4.13(0.16)	4.39(0.63)$E-1$	†1.67(0.67)$E-2$	†1.01(0.40)$E-2$		4.56(0.17)	4.60(0.17)
135	3.33(0.14)	†3.17(1.27)$E-1$	†1.22(0.49)$E-2$	†7.47(2.99)$E-3$		3.33(0.14)	3.67(0.19)
141	3.37(0.15)	†2.60(1.04)$E-1$	†8.86(3.56)$E-3$	†5.55(2.22)$E-3$		3.37(0.15)	3.65(0.18)
147	3.02(0.14)	†2.13(0.85)$E-1$	†6.45(2.59)$E-3$	†4.12(1.65)$E-3$		3.02(0.14)	3.24(0.16)
153	2.31(0.12)	†1.75(0.70)$E-1$	†4.70(1.89)$E-3$	†3.06(1.22)$E-3$		2.31(0.12)	2.49(0.14)
159	2.28(0.12)	†1.44(0.58)$E-1$	†3.43(1.38)$E-3$			2.28(0.12)	2.42(0.14)
165	2.25(0.12)	†1.18(0.47)$E-1$	†2.50(1.00)$E-3$			2.25(0.12)	2.37(0.13)
171	1.89(0.12)	†9.68(3.88)$E-2$				1.89(0.12)	1.98(0.12)
177	1.64(0.11)	†7.95(3.18)$E-2$				1.64(0.11)	1.72(0.11)
183	1.65(0.11)	†6.53(2.61)$E-2$				1.65(0.11)	1.72(0.11)
189	1.33(0.10)	†5.36(2.14)$E-2$				1.33(0.10)	1.38(0.10)
195	1.16(0.10)	†4.40(1.76)$E-2$				1.16(0.10)	1.20(0.10)

may be seen by comparing this column to the preceding column which does not contain the extrapolated cross sections. For most cases the angles measured were 30°, 50°, 70°, 90°, 110°, 130°, and 150°. In some cases 20° was also measured. For the Au target only four angles are presented, but for the case of 1.04 GeV/nucleon ^{20}Ne on U, measurements were made every 10° from 30° to 150°.

The complete set of data tables (116 pages) may be obtained from the Physics Auxiliary Publication Service.[49]

B. Single particle inclusive

Typical sets of double differential cross sections for protons and deuterons are shown in Figs. 8 and 9. These are the inclusive cross sections; the multiplicity-selected results will be presented in a later paper. The gap in the proton data at 120 MeV is due to the dead layer between the two pieces of germanium in the telescope. Toward lower energies the angular distributions become more isotropic, crowding the data together. These same data are transformed to graphs of invariant cross section versus momentum in Figs. 10 and 11. Because one divides by momentum to obtain the invariant cross section, the curves fall off faster with increasing momentum. Also, when one plots against momentum, the thin telescope region occupies a greater fraction of the abscissa.

Nagamiya *et al.*[50] have made similar measurements using a magnetic spectrometer, which

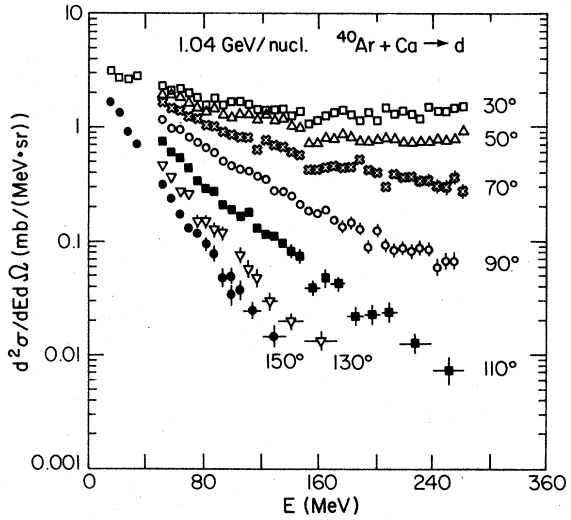

FIG. 9. Laboratory deuteron inclusive cross sections for the reaction of 1.04 GeV/nucleon ^{40}Ar on a Ca target. In the thin telescope region the data for only the extreme angles are shown.

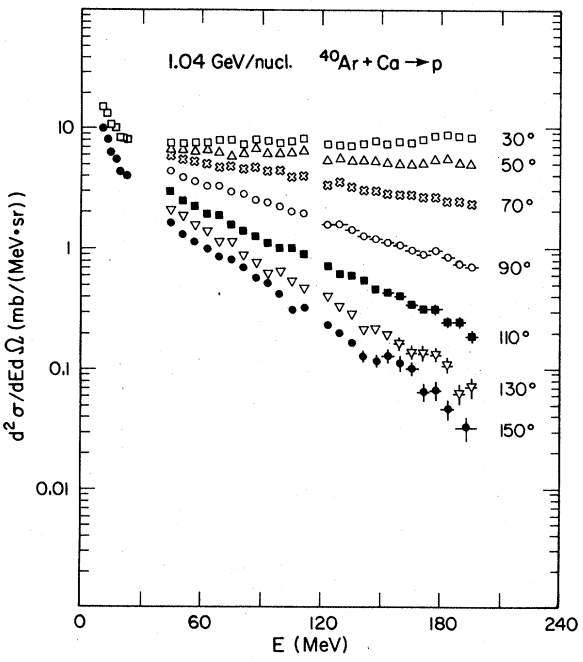

FIG. 8. Laboratory proton-inclusive cross sections for the reaction of 1.04 GeV/nucleon ^{40}Ar an a Ca target. In the thin telescope region only the most forward and backward angles are shown for clarity. The data for all the other angles fall between these extremes.

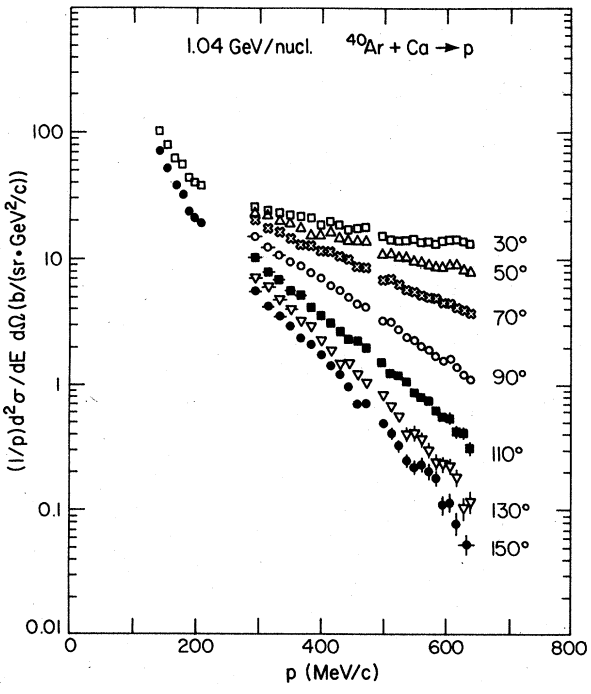

FIG. 10. Proton-inclusive invariant cross sections plotted versus laboratory momentum for the reaction of 1.04 GeV/nucleon ^{40}Ar on a Ca target. In the thin telescope region the data for only the extreme angles are shown.

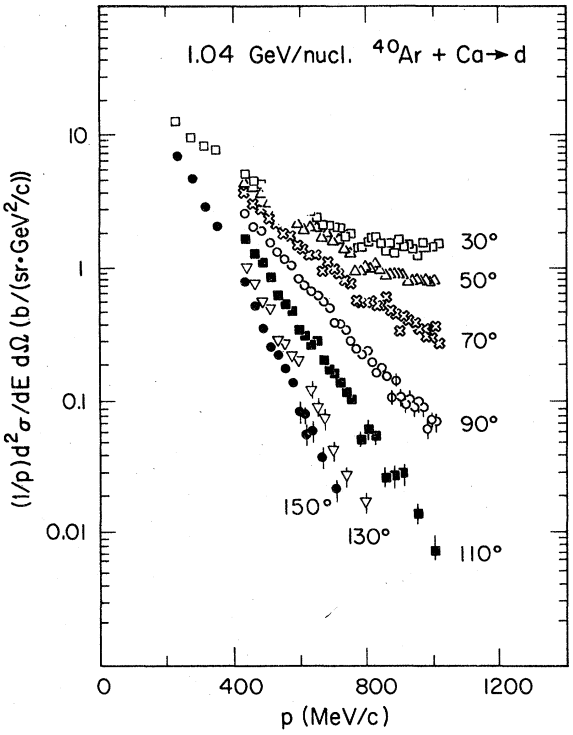

FIG. 11. Deuteron inclusive invariant cross sections plotted versus laboratory momentum for the reaction of 1.04 GeV/nucleon ^{40}Ar on a Ca target. In the thin telescope region the data for only the extreme angles are shown.

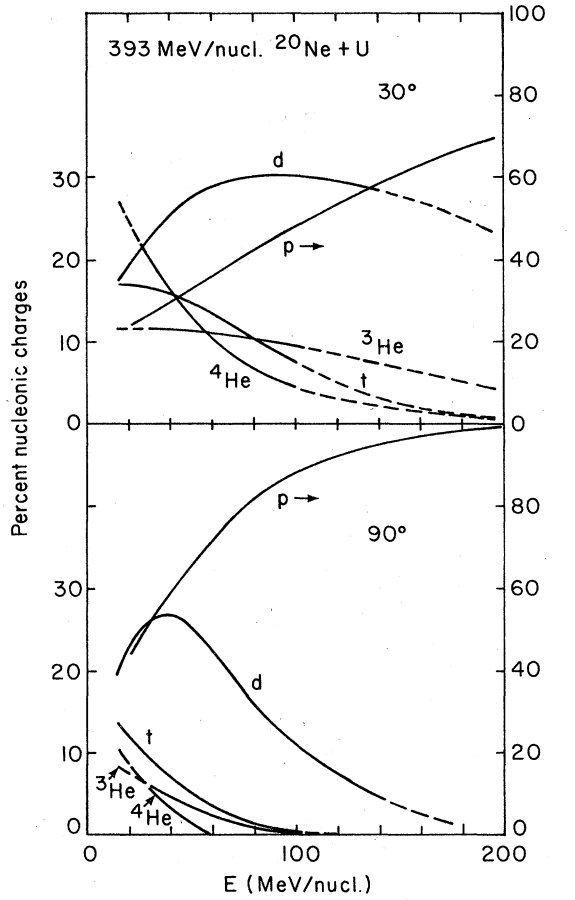

FIG. 12. The contribution of the protons and composite particles to the summed nucleonic charges, for 393 MeV/nucleon ^{20}Ne plus U. The percent contribution as a function of particle energy is shown at laboratory angles of 30° on the top and 90° on the bottom. The lines are dashed when based on extrapolated data. The vertical scale for the protons is compressed by a factor of 2 and shown on the right.

allowed them to make measurements extending to much higher particle momenta, typically up to 2 GeV/c. Unfortunately, there are no target-projectile energy combinations where an exact comparison of the two sets of data can be made. With 400 MeV/nucleon ^{20}Ne ions our proton cross sections from U are only about 10% higher than from Au. The Nagamiya *et al.* proton cross sections from Pb in the region of 500 to 600 MeV/c are about 35% lower than ours from Au. We believe this is approximately within our combined normalization errors. Below about 400 MeV/c, their data deviate more, presumably because of multiple scattering losses in their magnetic spectrometer at the lower end of their range of observation.

The summed nucleonic charges are presented in the data tables. Figure 12 shows how the various particles contribute to this sum. The proton contribution approaches 100% only for high energies at large angles. At low energies at forward angles it drops as low as 25%. The fractional contribution of the deuterons first rises with deuteron energy, simply because the contributions of the other particles are falling faster than the deuteron. At high deuteron energy, especially at back angles, the deuteron contribution falls off. It can be seen that the heavier the fragment, the faster the falloff with energy, but that t, ^{3}He, and ^{4}He all make comparable contributions. It is doubtful that still heavier fragments would make any significant contribution in this energy range. For the two other cases where we have He fragment data, 241 and 2095 MeV/nucleon ^{20}Ne on U, the relative contributions of the various particles is very similar to that shown in Fig. 12. The variation with angle is shown in more detail in Fig. 13. Except for low-energy deuterons, the fractional contribution of the composite particles falls off at large angles, especially for high-energy particles. If we think in terms of the coalescence model,[1,3] it appears that the proton yield is appreciably depleted by the formation of

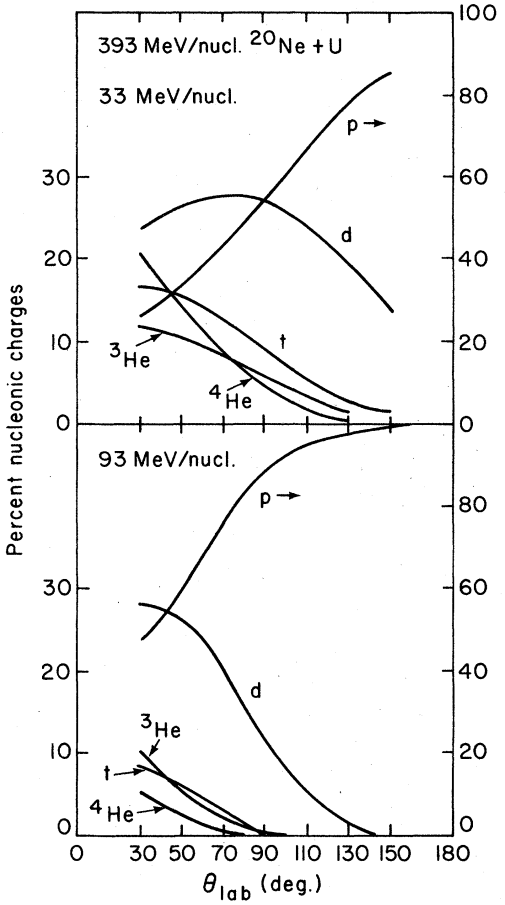

FIG. 13. The percent contribution of the protons and composite particles to the nucleonic charges as a function of laboratory angle, for low-energy particles (33 MeV/nucleon) on the top, and high energy particles (93 MeV/nucleon) on the bottom. The vertical scale for the protons is compressed by a factor of 2 and is shown on the right.

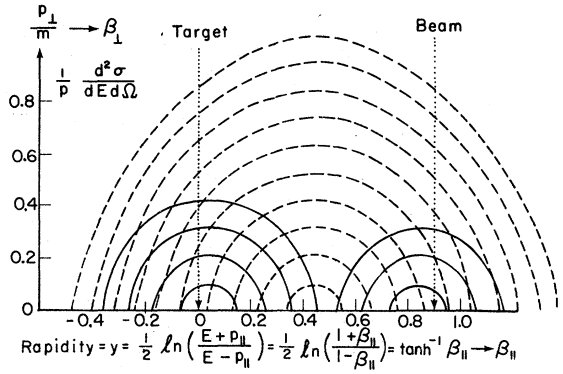

FIG. 14. Schematic plot of contours of constant invariant cross section versus rapidity and perpendicular momentum divided by the mass of the particle. The symbol E in the definition of rapidity represents total energy, not kinetic energy, as in the double differential cross section. The symbols p and β represent momentum and velocity in units of c. The laboratory rapidity is defines as zero. The case illustrated is for projectile rapidity of 0.9 which corresponds to 400 MeV/nucleon. The contours are drawn for momentum steps of 100 MeV/c.

composite particles. In fact, at low energies and forward angles the deuteron yield is depleted by the heavier composites.

Fitting the data with coalescence theory was attempted. However, with the present accurate data it was found that p_0, the radius of the coalescence volume in momentum space, was not constant with fragment energy. This is not surprising in view of the high density of particles in momentum space, and of the fact that the theory which we have been using assumes a low density approximation.

An informative way to present[1] inclusive data is to make a contour plot, as illustrated schematically in Fig. 14. The abscissa is the rapidity, which is a velocity-like variable defined in the figure. It has the property that, in transforming to a moving system, one simply adds linearly the rapidity of the moving system. Nonrelativistically it approaches the velocity parallel to the beam in units of c. The ordinate is the perpendicular momentum divided by the mass of the particle. This is a relativistic invariant which nonrelativistically approaches the velocity perpendicular to the beam in units of c. Plotted are contours of constant invariant cross sections. Such a plot is invariant with respect to Lorentz transformations, except for a shift of the rapidity axis. Illustrated are three sets of contours, each set calculated assuming isotropic emission in a moving system. The contours centered near zero rapidity are meant to represent particles from the target spectator, and those centered near the beam rapidity, the projectile spectator. Contours centered at an intermediate rapidity and extending out to high perpendicular momentum are meant to represent the participants from a fireball-type system. Notice that at high perpendicular momentum the contours are no longer circular, but tend to peak slightly. In the case of an equal mass target and projectile there must be symmetry about the mean rapidity of the beam and target. Lines of constant laboratory angle are shown in Fig. 2. Such contour plots as Fig. 14 are a relatively model-independent way of assessing the various contributing sources to the experimental data.

An example of such a plot is shown in Fig. 15 for ^{20}Ne on U. It can be seen that at low momentum the contours center near the rapidity of the target, but at high momentum they tend to center toward the intermediate rapidity region.

The reaction of ^{40}Ar with Ca is very nearly an

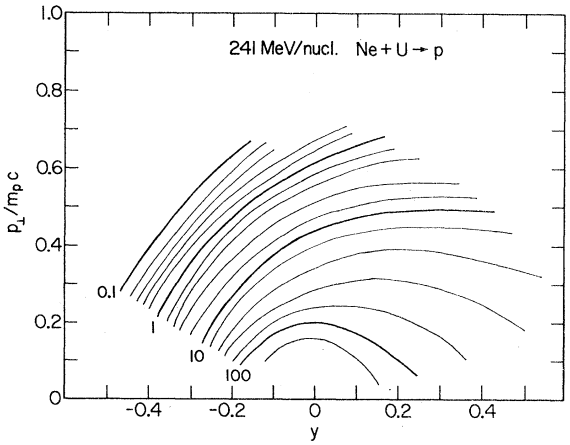

FIG. 15. For protons from the reaction of 241 MeV/nucleon ^{20}Ne on U, contours of constant invariant cross section in units of b/(sr GeV^2/c) are shown. There are five logarithmically spaced contours for each decade which is labeled. The rapidity of the projectile is 0.70.

equal mass collision because natural Ca is 97% ^{40}Ca. Although Ar has 10% fewer protons than Ca, we have assumed that the system is symmetric and that the data can be reflected about the mean rapidity of the projectile and the target. Thus, the case of ^{40}Ar plus Ca is particularly interesting because it is possible to examine a relativistic nuclear collision in its center of mass. An example of an ^{40}Ar plus Ca system is shown in Fig. 16 for protons and in Fig. 17 for deuterons. The contours at high perpendicular momentum center at the mid-rapidity, while the low perpendicular momentum contours are beginning to pinch into the projectile and target regions of a peripheral collision. However, for most of the region measured, the protons appear to originate from the mean rapidity of target and projectile, which is the center of mass of the system and also the center of

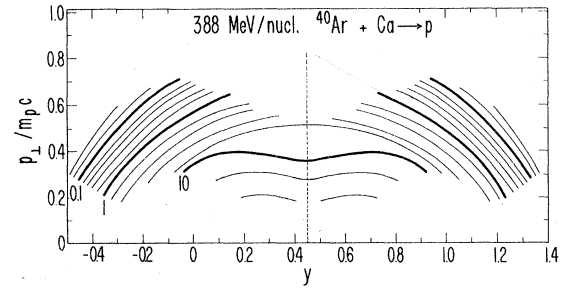

FIG. 16. Contours of constant invariant cross section for protons from the reaction of 388 MeV/nucleon ^{40}Ar with a Ca target. The rapidity of the projectile is 0.88 and the data on the left have been reflected about the mean rapidity of the target and projectile to produce the right-hand side of the figure.

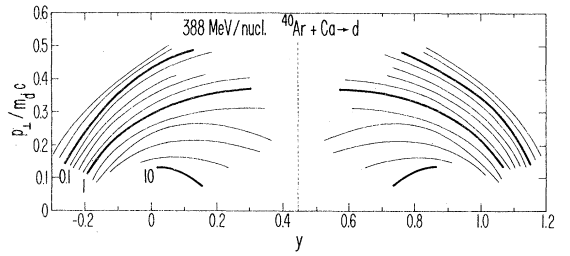

FIG. 17. Contours of constant invariant cross section for deuterons from the reaction of 388 MeV/nucleon ^{40}Ar with a Ca target.

the fireball frame for all impact parameters. For unequal target and projectile masses the velocity of the fireball frame would depend upon the impact parameter.

In Fig. 18 we have replotted the data in terms of the longitudinal momentum in the center of mass and the perpendicular momentum. Although the contours appear approximately the same, the axes are very different. At higher bombarding energies there is a greater distortion of the contours in this transformation due to relativistic effects. From the graph, momentum spectra in the center of mass were obtained and are shown in Fig. 19. The near independence with center-of-mass angle indicates that there is mainly an isotropic source at the center of mass. The dropping down of the low-momentum 90° curve corresponds to the dip in the contour plot. However, when the projectile energy is raised to 1.04 GeV/nucleon the situation is quite different, as seen in Fig. 20. It appears that, over the region measured, there is approximate isotropy for high momentum protons, but at low momentum they are quite strongly forward-backward peaked in the center of mass, corresponding more closely to isotropy in the target and projectile frames, as shown already in Fig. 10.

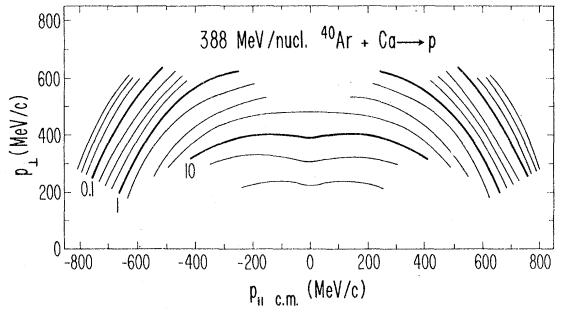

FIG. 18. Contours of constant invariant cross section versus the center of mass longitudinal momentum and perpendicular momentum. The data are for protons from the reaction of 388 MeV/nucleon ^{40}Ar on a Ca target and have been reflected about a center of mass angle of 90°. There are four logarithmically spaced contours for each decade which is labeled.

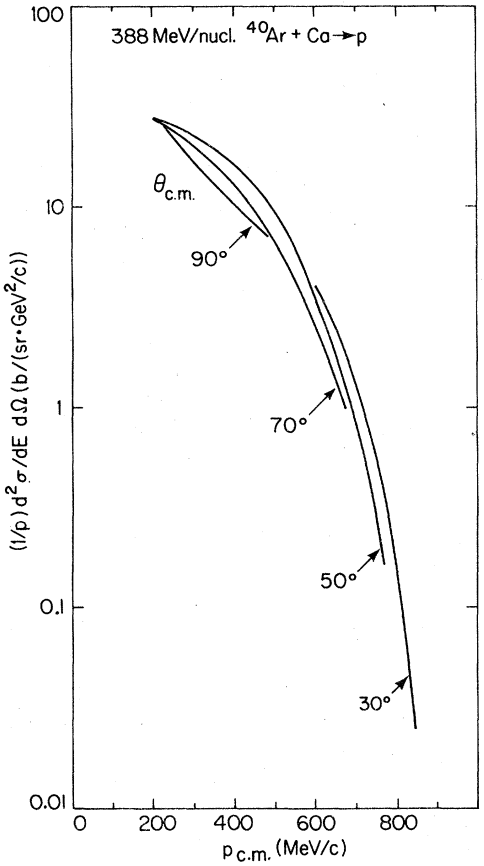

FIG. 19. Invariant cross section versus momentum in the center of mass for different center of mass angles. Since symmetry was assumed, the curves also refer to the supplements of the indicated angles. The data are for protons from the reaction of 388 MeV/nucleon ^{40}Ar on a Ca target.

C. Multiplicities

The average associated multiplicties were extracted from the data as described above. We will discuss their dependence on the size of the projectile and target, on the energy of the projectile, and on the type of triggering particle and its angle.

A convenient parameter for plotting the variation of multiplicity with target and projectile sizes is the average number of proton participants calculated in the clean-cut or fireball geometry.

This is given by[24]

$$\frac{\pi r_0^2(Z_t A_p^{2/3} + Z_p A_t^{2/3})}{\pi r_0^2 (A_p^{1/3} + A_t^{1/3})^2} . \tag{7}$$

The numerator consists of the number of protons in the target times the area of the projectile, plus the number of protons in the projectile times the area of the target, while the denominator is the geometrical reaction cross section. In Fig. 21

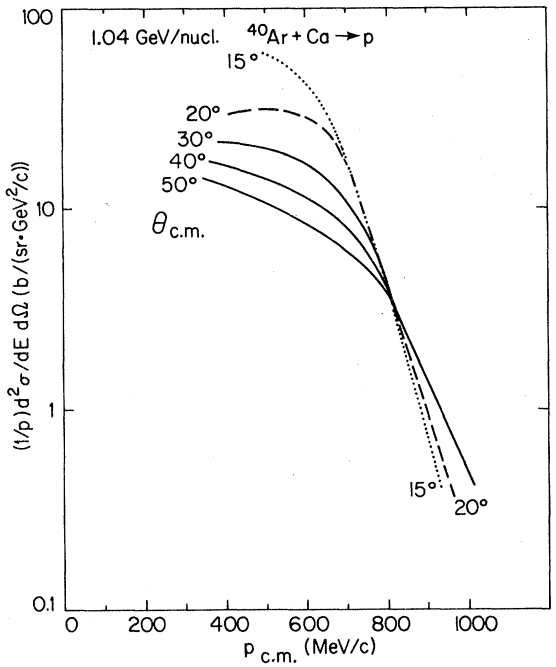

FIG. 20. Invariant cross section versus momentum in the center of mass for protons from the reaction of 1.04 GeV/nucleon ^{40}Ar on a Ca target. The curves also refer to the supplements of the indicated angles.

the average associated multiplicties observed for four different projectile energies are shown. These are the multiplicities associated with a proton in the thick telescope at 90° to the beam. More points are plotted than indicated in Table I because in several cases a small amount of data was taken only at 90° just to study this relationship. Interestingly, the data are approximately linear as a function of the average number of proton partici-

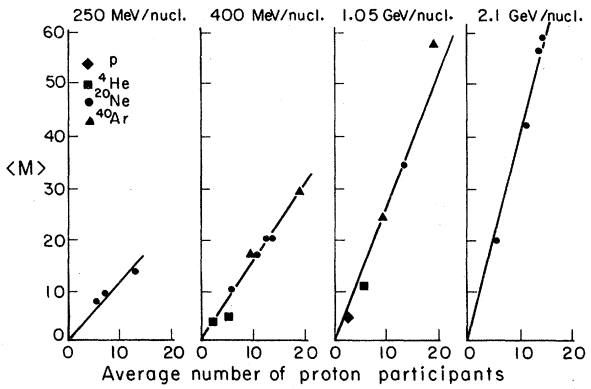

FIG. 21. The average associated multiplicities obtained from the scintillation paddles plotted versus the average number of proton participants calculated in the clean-cut geometry model. Data from many different target-projectile combinations are shown at four bombarding energies. The lines are drawn through the data.

pants, even though very different target-projectile combinations are plotted. At 250 MeV/nucleon the slope is approximately one. However, the lines increase in slope with bombarding energy and thus are considerably above the clean-cut geometry predictions at the higher energies. Let us examine these slopes for the Ne plus U cases in Fig. 22. The four circles labeled "from paddles" are the associated multiplicties at the four bombarding energies from Fig. 21. Another way to calculate multiplicities which was described above is from the telescope data by taking the total single-particle cross section divided by the geometric reaction cross section (squares in Fig. 21). For Ne on U a reaction cross section of 4.1 b[51] was used. The results, which are also plotted, are a factor of 2 lower than the associated multiplicties from the paddle array. Clearly, requiring a high-energy proton at 90° in the telescope biases the paddle multiplicities to higher values. Quantitative calculations of this effect[1] in the fireball framework have been done by Cecil, Das Gupta, and Mekjian.[52]

The curves labeled "fireball" and "firestreak" were calculated[9] by integrating the yield of particles at laboratory angles greater than 10° with sufficient energy to penetrate the wall of the scattering chamber. These calculations are of multiplicities (not associated multiplicties) and are to be compared with the data from single-particle cross sections. The theoretical curves rise quickly at low bombarding energy as the particles obtain sufficient energy to penetrate the wall of the scattering chamber. They continue to rise at high bombarding energies because of pion production, which is only somewhat compensated for by composite particle formation. The firestreak model includes a surface thickness which makes its multiplicities higher than the fireball. The fireball geometrical factor for the average number of proton participants, calculated by Eq. (7), is indicated by the horizontal line. Although the rise of the measured average multiplicties with bombarding energy is predicted by the firestreak curve we will see that the double differential cross sections are not fit very well.

A surprising result is observed in Fig. 23 where the associated multiplicities for all the uranium target cases are plotted versus the total kinetic energy (not the energy/nucleon) of the projectiles. This apparently smooth relationship indicates that increasing the energy/nucleon of the projectile is just as important as increasing the mass of the projectile, as regards the effect on the mean multiplicities. Also, there appears to be no strong effect relative to the pion threshold. In fact, not

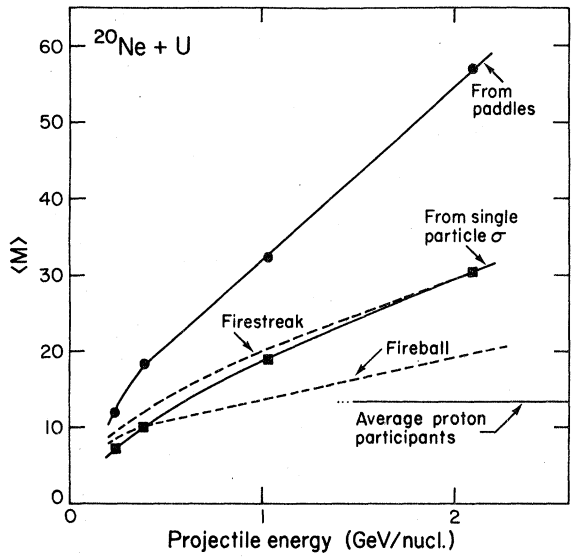

FIG. 22. The average multiplicities for the Ne+U systems as a function of the projectile energy. Experimental results from the paddles and the integrated single-particle cross sections are shown as points. Also indicated are the calculations based on the fireball and firestreak models, as well as the average number of proton participants from the clean-cut geometrical model.

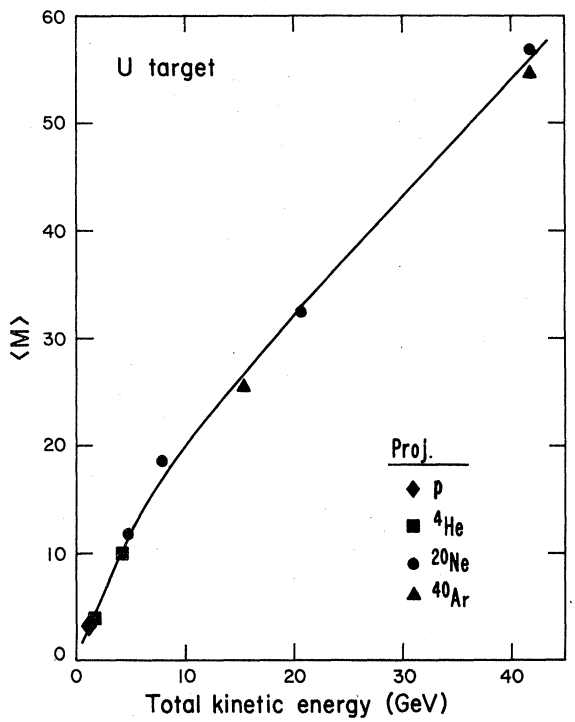

FIG. 23. Average associated multiplicities plotted versus the total kinetic energy of various projectiles on a uranium target. The curve is drawn through the points.

only the means, but the observed multiplicity distributions are the same, as is shown in Fig. 24 for two projectiles with 42 GeV of kinetic energy.

These multiplicity distributions include charged particles removed from the target, and thus should be somewhat inversely related to radiochemical mass yield curves which represent the mass distribution of the target residues. For mass yield curves, the importance of the total kinetic energy has already been pointed out by comparing heavy ions with protons for the spallation of copper[53] and tantalum.[54] For Cu the slopes of the mass yield curves with incident p, ^{4}He, ^{12}C, ^{14}N, and ^{40}Ar were found[53] to be a smooth function of the total kinetic energy. However, above 1 GeV the mass yield curves are independent of projectile energy[55] and therefore the effect is not as striking as in Fig. 23 where there is a strong energy dependence.

The multiplicities presented so far have been associated with protons detected in the telescope at 90° to the beam. There is some dependence with angle of the telescope, as is shown in Fig. 25. Most of the cases studied exhibited behavior like the top and bottom curves, with the falloff

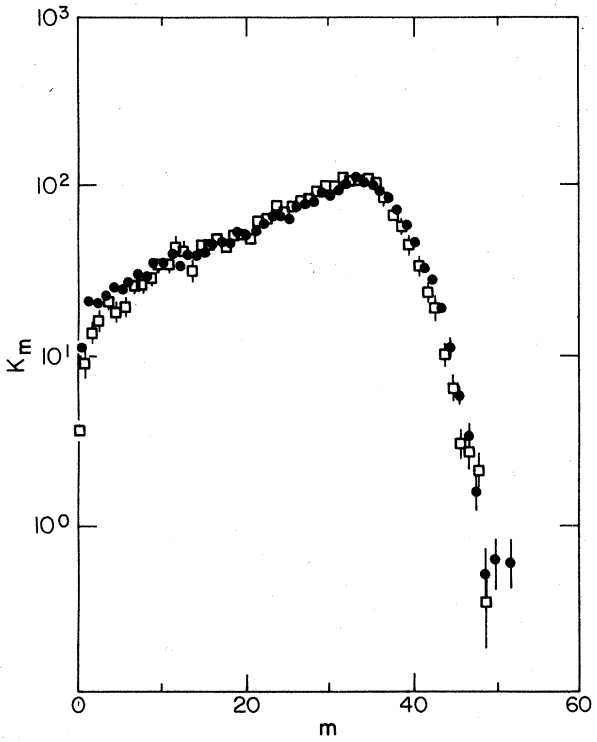

FIG. 24. Coincidence probability distributions for 1.05 GeV/nucleon ^{40}Ar and 2.1 GeV/nucleon ^{20}Ne on a uranium target. Both projectiles have 42 GeV total kinetic energy. The distributions are of the number of the 80 scintillation paddles which fired.

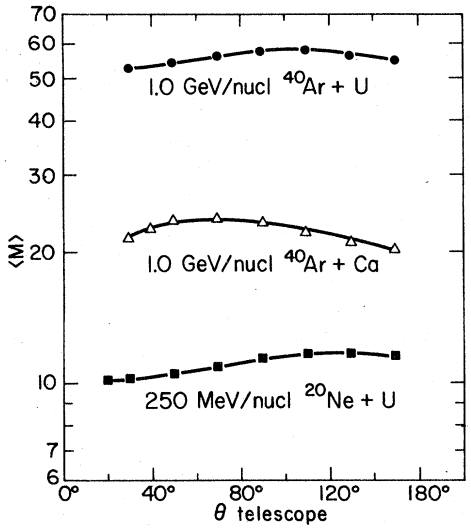

FIG. 25. Average associated multiplicity as a function of the angle of the proton trigger.

at forward angles most pronounced at the low bombarding energies. This is consistent with the effect being due to the low multiplicity peripheral collisions preferentially populating the low-energy region at forward angles.

The only curve measured which does not drop at forward angles is the middle curve in Fig. 25 for the case of 1.0 GeV/nucleon ^{40}Ar plus Ca. In fact, it has the opposite trend. We can examine this case in more detail in Fig. 26, which is a contour plot of mean multiplicity. Here we cannot only see the variation with angle of the trigger proton, but also with its momentum. One can see that in the target region, which would be dominated by peripheral collisions, the multiplicity is low, while as the momentum of the trigger particle increases, the multiplicity increases.

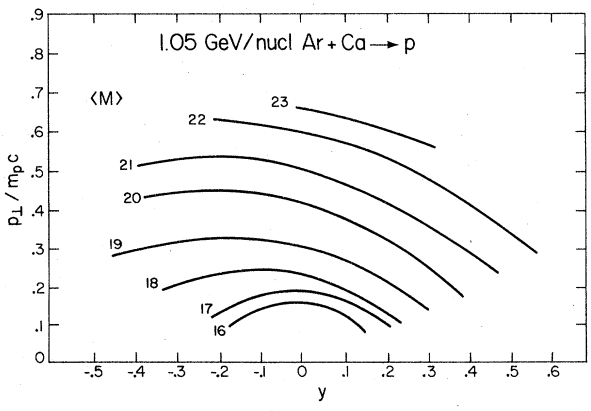

FIG. 26. Contours of constant average associated multiplicity for the case of 1.05 GeV/nucleon ^{40}Ar on Ca as a function of the perpendicular momentum and rapidity of the trigger proton.

The variation of multiplicity with the type of triggering particle as identified in the telescope is shown in Fig. 27. The lower curve for protons is the same as the upper curve in Fig. 22. The multiplicities increase somewhat with the mass of the trigger particle, but the effect is not dramatic. An increase is reasonable because the higher the multiplicity, the higher the probability of nucleons coalescing into composite particles.

D. Correlations

The azimuthal correlations of charged particles in the multiplicity array relative to a proton in the telescope have been investigated. The angles involved are shown in Fig. 7. The results for 1.0 GeV protons on uranium are shown on the top of Fig. 28. The peak on the left means that when a proton is observed in a telescope at 90° to the beam there is a positive correlation for observing charged particles on the opposite side of the beam line at a small angle to the beam. This is what one would call quasifree scattering and is not all unreasonable for this case of 1 GeV incident protons. The peaks in the other two curves at azimuthal angles of 180° for larger angles to the beam are harder to understand. It can be seen that for incident ^{4}He ions the quasifree peak disappears and the other peaks are also almost gone. For all heavier projectiles no clear peaks were

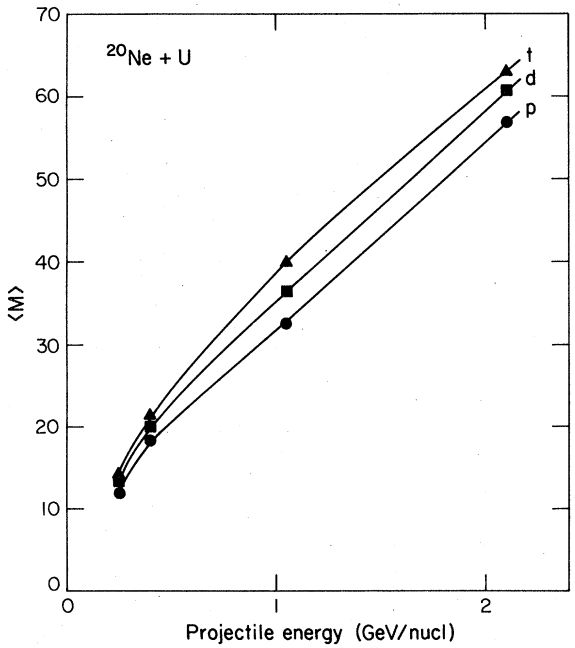

FIG. 27. Average associated multiplicities for ^{20}Ne on U as a function of projectile energy. The trigger particles are protons, deuterons, and tritons.

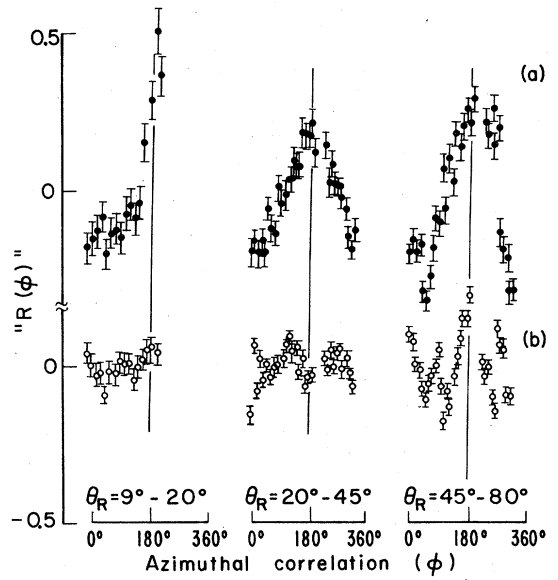

FIG. 28. Azimuthal correlations for three rings of the multiplicity array representing different polar angular intervals with respect to the beam. The correlations are with respect to a proton in the telescope at a polar angle (θ_T) of 90° to the beam and which define an azimuthal angle (ϕ) of 0°. The vertical lines are at ϕ=180°. (a) 1 GeV protons on U. (b) 1 GeV/nucleon ^{4}He ions on U.

observed. However, even for the heavier projectiles some structure remained in the data, which was partly determined to be due to shadowing of the scintillator paddles by the telescope and its associated electronic and cryogenic equipment inside the scattering chamber. Also, one would expect on simple statistical arguments[56] that a peak in an angular correlation would decrease with the square root of the multiplicity. Thus, a more refined method of analysis is needed for heavier projectiles, in which the statistical effect combined with the residual shadowing effects is taken into account, thus enhancing the sensitivity for detecting underlying correlations.[57]

IV. DISCUSSION AND SUMMARY

No attempt will be made to make an exhaustive comparison of our new data with the many models which have been proposed. However, since our old data was largely responsible for stimulating the thermal models, a comparison will be made with the firestreak calculations[9] to show the limits to which these simple models agree with the data.

Figure 29 shows the double differential cross section for protons from the reactions of Ne with U at energies of 241, 393, 1045, and 2095 MeV/nucleon. For reasons of clarity, only three angles (30°, 90°, 150°) are presented to illustrate the

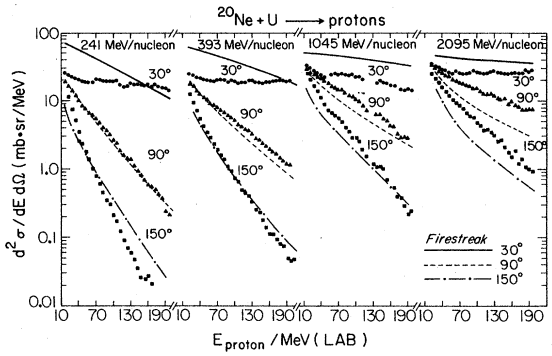

FIG. 29. Laboratory proton-inclusive cross sections from the interaction ^{20}Ne on a U target at 241, 393, 1045, and 2095 MeV/nucleon. The lines are from a firestreak calculation (Ref. 9).

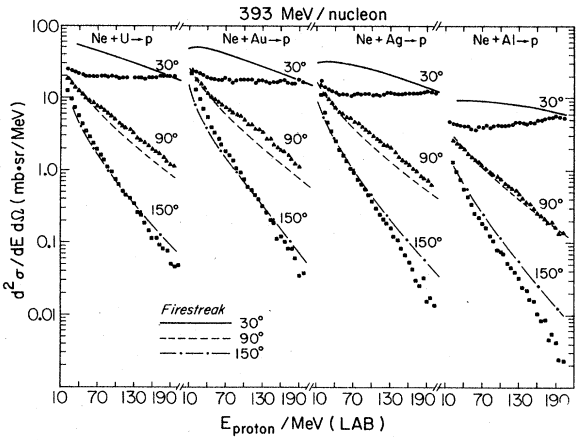

FIG. 30. Proton-inclusive cross sections from the interaction of 393 MeV/nucleon ^{20}Ne on U, Au, Ag, and Al at selected angles. The lines are the firestreak model predictions.

trends in the comparison with the firestreak calculation. At all incident energies the forward angle data are in strong disagreement with theory. The shapes of the 30° data are very similar for all incident energies. Recently published neutron data[59] are in better agreement with this model at forward angles than the proton data. Gyulassy[60] attributes this to the fact that the Coulomb repulsion is not properly considered in the present firestreak model. The back angles are fairly well described, but only at the low bombarding energies. Even there the slope is different, with the data falling off steeper than the theory predictions. In general it can be seen that at energies above 40 MeV the thermal model underestimates the experimental cross section at large angles.

Concentrating on the energy of 393 MeV/nucleon, where the agreement between theory and data is still reasonable at large angles, the target dependence can be studied for Ne induced reactions. Figure 30 shows proton double differential cross sections from reactions of 393 MeV/nucleon ^{20}Ne with targets of U, Au, Ag, and Al. One striking feature, the near equal shape of the 90° spectra for all target nuclei, is well described by the firestreak model. But again, the forward angle data are in total disagreement with the theory for all target nuclei. All back angles fall off more steeply at higher proton energy than the calculations show.

These comparisons clearly show that the firestreak model with diffuse nuclear surface predicts too much yield at low proton energies at forward angles, and on the other hand, it underestimates strongly, with increasing bombarding energies, the cross section at large angles. In general, one might even question here the firestreak kinematics which assumes that the probability distribution for finding a nucleon in the surface can be used as an actual matter density. This failure of taking into account the discreteness of nucleons implies that there are streaks with less than a nucleon from either the projectile or the target nucleus, thus causing unrealistic kinematical effects. However, the fair agreement of this model with data at 90° (where the kinematical effect is smallest) for bombarding energies from 241 MeV/nucleon to 1045 MeV/nucleon is an indication of the strong thermal component in these reactions. It will be interesting to see whether an accurate treatment of the Coulomb force in the firestreak model will reduce some of the discrepancies with the data.

The firestreak model, simultaneously with the proton double differential cross sections, predicts double differential cross sections for π, d, t, and alpha particles. The comparison with the π data has been made in Ref. 34. The fit to our d and t data is similar to that for the protons, with the largest discrepancy occurring at low energies under forward angles. Compared to the quality of distorted-wave Born approximation (DWBA) fits at low-energy nuclear physics, it is still remarkable that the gross features of the cross section can be predicted for π, p, d, and t by such a simple thermal model.

In most other theoretical models there is no provision made to describe any fragment other than proton or neutron. Thus the emission of light fragments like ^{4}He has to be folded back into the emission of two protons and two neutrons. Therefore, to make a comparison with these models possible, the summed nucleonic charges are presented in Fig. 31 for the reaction of 241 MeV/nucleon ^{20}Ne plus U. Comparison is made with the intranuclear cascade calculations of Fraenkel and Yariv[21] and the two-fluid hydrody-

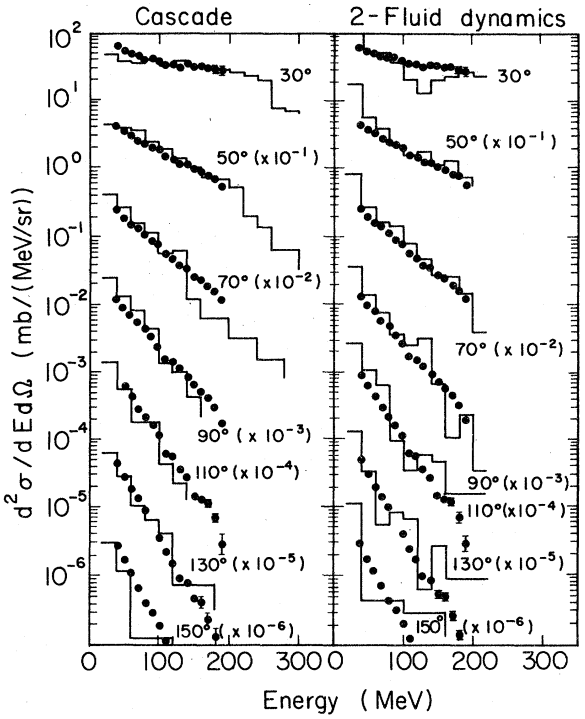

FIG. 31. The points represent the summed nucleonic charges for the reaction of 241 MeV/nucleon ^{20}Ne on U. The histograms on the left are from a cascade calculation (Ref. 21) and on the right from a two-fluid hydrodynamic calculation (Ref. 27).

namic calculations of Amsden, Goldhaber, Harlow, and Nix.[27] One is a microscopic and the other a macroscopic calculation. The agreement is excellent for these two extreme models, showing, however, the insensitivity of the inclusive cross section to the details of the reaction mechanism. More exclusive data has to be used to probe the dynamics of the interaction. One type of this kind of data, the multiplicity-selected proton-inclusive cross sections, are discussed in a separate paper.[61] Another kind of more exclusive data are the associated multiplicity distributions. Recent calculations of the associated charged-particle multiplicity in the cascade model[21] agreed in the mean values but disagreed in the shape of the multiplicity distributions. It was observed for the associated multiplicities (Fig. 24) that besides the mean value, the shape of their distributions is also nearly the same for different incident projectiles on a U target, as long as the projectile has the same total kinetic energy. The importance of the total kinetic energy in near central collisions has also been found in studies of low-energy fragments which are produced only in violent reactions.[58]

Thus it becomes clear that the earlier spectator-participant picture may hold only for very peripheral collisions. In contrast, nuclear collisions leading to the emission of the fragments studied here are of a violent nature where the total kinetic energy of the projectile dominates the decay pattern of the final system. It is interesting to see whether the cascade model or the hydrodynamical model can describe this effect. In the search for exotic effects in particular, high-multiplicity selected data must be compared with calculations selected for central collisions.

ACKNOWLEDGMENTS

This work was supported by the Nuclear Physics Division of the U.S. Department of Energy under Contract No. W-7405-ENG-48 and by the Bundesministerium für Forschung und Technologie, West Germany. In particular we would like to acknowledge the support of R. Bock for this project. We are grateful to H. A. Grunder, R. J. Force, J. R. Alonso, H. M. Ellison, and the rest of the Bevalac staff for their appreciable support. We would like to thank E. E. Haller, R. C. Cordi, J. T. Walton, D. F. Malone, V. A. Fletcher, and C. D. Buresh for their help in developing the experimental apparatus. We would also like to thank Z. Fraenkel, Y. Yariv, and J. R. Nix for providing us with the results of their theoretical calculations.

*Present address: Bell Laboratories, Reading, Pennsylvania 19604.
†Present address: Geselleschaft für Reaktorsicherheit, Köln.
‡Present address: DPhN/ME, CEN Saclay, 91190 Gif-sur-Yvette, France.
§Present address: Institut de Physique Nucleaire, 91406 Orsay, France.
‖Present address: Bell Laboratories, Murray Hill, New Jersey 07974.
¶Present address: Schlumberger-Doll Research Center, P.O. Box 307, Ridgefield, Connecticut 06877.
**Present address: Institut des Sciences Nucleaires, 38044 Grenoble, France.
††Present address: Argonne National Laboratory, Argonne, Illinois 60439.

[1] J. Gosset, H. H. Gutbrod, W. G. Mayer, A. M. Poskanzer, A. Sandoval, R. Stock, and G. D. Westfall, Phys.

Rev. C 16, 629 (1977).
[2]G. D. Westfall, J. Gosset, P. J. Johansen, A. M. Poskanzer, W. G. Meyer, H. H. Gutbrod, A. Sandoval, and R. Stock, Phys. Rev. Lett. 37, 1202 (1976).
[3]H. H. Gutbrod, A. Sandoval, P. J. Johansen, A. M. Poskanzer, J. Gosset, W. G. Meyer, G. D. Westfall, and R. Stock, Phys. Rev. Lett. 37, 667 (1976).
[4]J. I. Kapusta, Phys. Rev. C 16, 1493 (1977).
[5]A. Mekjian, Phys. Rev. Lett. 38, 640 (1977); Phys. Rev. C 17, 1051 (1978).
[6]R. Bond, P. J. Johansen, S. E. Koonin, and S. Garpman, Phys. Lett. 71B, 43 (1977).
[7]S. Das Gupta, Phys. Rev. C 18, 2773 (1978).
[8]W. D. Myers, Nucl. Phys. A296, 177 (1978).
[9]J. Gosset, J. I. Kapusta, and G. D. Westfall, Phys. Rev. C 18, 844 (1978).
[10]M. Gyulassy and S. K. Kauffman, Phys. Rev. Lett. 40, 298 (1978).
[11]S. Das Gupta, Phys. Rev. Lett. 41, 1450 (1978).
[12]N. K. Glendenning and Y. Karant, Phys. Rev. Lett. 40, 374 (1978); N. K. Glendenning, in *Theoretical Methods in Medium-Energy and Heavy-Ion Physics*, edited by K. W. McVoy and W. A. Friedman (Plenum, New York, 1978), p. 451.
[13]J. P. Bondorf, S. I. A. Garpman, and J. Zimanyi, Nucl. Phys. A296, 320 (1978).
[14]Y. Kitazoe and M. Sano, Lett. Nuovo Cimento 22, 153 (1978).
[15]P. J. Siemens and J. O. Rasmussen, Phys. Rev. Lett. 42, 880 (1979).
[16]G. Mantzouranis, Phys. Rev. C 18, 2227 (1978).
[17]Meng Ta-Chung and E. Moeller, Phys. Rev. Lett. 41, 1352 (1978).
[18]A. A. Amsden, J. N. Ginocchio, F. H. Harlow, J. R. Nix, M. Danos, E. C. Halbert, and R. K. Smith, Jr., Phys. Rev. Lett. 38, 1055 (1977).
[19]M. Gyulassy, Fisika 9, 623 (1977), Suppl. 4.
[20]J. R. Nix, Prog. Part. Nucl. Phys. (to be published).
[21]Z. Fraenkel and Y. Yariv, Phys. Rev. C 20, 2227 (1979).
[22]R. K. Smith and M. Danos, Fall Creek Falls Conference Proceedings (ORNL Report No. CONF-770602, 1977), p. 363.
[23]J. D. Stevenson, Phys. Rev. Lett. 41, 1702 (1978).
[24]J. Hufner and J. Knoll, Nucl. Phys. A290, 460 (1977).
[25]J. Randrup, Phys. Lett. 76B, 547 (1978); Nucl. Phys. A316, 509 (1979).
[26]A. A. Amsden, F. H. Harlow, and J. R. Nix, Phys. Rev. C 15, 2059 (1977).
[27]A. A. Amsden, A. S. Goldhaber, F. H. Harlow, and J. R. Nix, Phys. Rev. C 17, 2080 (1978).
[28]J. P. Vary (unpublished).
[29]S. E. Koonin, Phys. Rev. Lett. 39, 680 (1977).
[30]R. L. Hatch and S. E. Koonin, Phys. Lett. 81B, 1 (1979).
[31]A. S. Goldhaber and H. H. Heckman, Annu. Rev. Nucl. Sci. 28, 161 (1978).
[32]*Symposium on Relativistic Heavy-Ion Research, GSI Darmstadt, March 1978*, GSI Report No. GSI-P-5-78, 1978.
[33]*Proceedings of the Fourth High-Energy Heavy-Ion Summer Study, July, 1978*, Lawrence Berkeley Laboratory, California, LBL Report No. LBL-7766.
[34]K. L. Wolf, H. H. Gutbrod, W. G. Meyer, A. M. Poskanzer, A. Sandoval, R. Stock, J. Gosset, C. H. King, G. King, Nguyen Van Sen, and G. D. Westfall, Phys. Rev. Lett. 42, 1448 (1979).
[35]Designed by William Holley, Gerry Schnurmacher, and Arthur Zingher.
[36]W. H. Barkas and M. J. Berger, National Aeronautics and Space Administration Report No. NASA SP-3013 (1964).
[37]W. P. Jesse, Radiat. Res. 33, 229 (1968).
[38]A. M. Poskanzer, G. W. Butler, and E. K. Hyde, Phys. Rev. C 3, 882 (1971).
[39]M. Q. Makino, C. N. Waddell, and R. M. Eisberg, Nucl. Instrum. Methods 60, 109 (1968).
[40]D. F. Measday and C. Richard-Serre, Nucl. Instrum. Methods 76, 45 (1969).
[41]K. G. R. Doss, private communication.
[42]G. B. Hagemann, R. Broda, B. Herskind, M. Ishihara, S. Ogaza, and H. Ryde, Nucl. Phys. A245, 166 (1975).
[43]D. G. Sarantites, J. H. Barker, M. L. Halbert, D. C. Hensley, R. A. Dayras, E. Eichler, N. R. Johnson, and S. A. Gronemeyer, Phys. Rev. C 14, 2138 (1976).
[44]W. Kohl, D. Kolb, and I. Giese, Z. Phys. A285, 17 (1978).
[45]D. Andersen, R. Baner, G. B. Hagemann, M. L. Halbert, B. Herskind, M. Neiman, H. Oeschler, and H. Ryde, Nucl. Phys. A295, 163 (1978).
[46]W. J. Ockels, Z. Phys. A286, 181 (1978).
[47]M. Abramowitz and I. A. Stegun, *Handbook on Mathematical Functions* (Dover, New York, 1965), p. 821.
[48]S. E. Koonin, Phys. Lett. 70B, 43 (1977).
[49]See AIP document No. PAPS PRVCA 21-1321-118 for 118 pages of data tables. Order by PAPS number and journal reference from American Institute of Physics, Physics Auxiliary Publications Service, 335 East 45th Street, New York, New York 10017. The prices is $3 for microfiche of $18.20 for photocopies. Airmail additional. Make checks payable to the American Institute of Physics. This material also appears in *Current Physics Microfilm*, the monthly microfilm edition of the complete set of journals published by AIP, on frames immediately following this journal article.
[50]M.-C. Lemaire, S. Nagamiya, O. Chamberlain, G. Shapiro, S. Schnetzer, H. Steiner, and I. Tanihata, unpublished data.
[51]P. J. Karol, Phys. Rev. C 11, 1203 (1975).
[52]G. Cecil, S. Das Gupta, and A. Mekjian, Phys. Rev. C 20, 1021 (1979).
[53]J. B. Cumming, R. W. Stoenner, and P. E. Haustein, Phys. Rev. C 14, 1554 (1976).
[54]D. J. Morrissey, W. Loveland, and G. T. Seaborg, Z. Phys. A289, 123 (1978).
[55]J. B. Cumming, P. E. Haustein, T. J. Ruth, and G. J. Virtes, Phys. Rev. C 17, 1632 (1978).
[56]S. E. Koonin, private communication.
[57]L. Wilson, private communication.
[58]W. G. Meyer, H. H. Gutbrod, Ch. Lukner, and A. Sandoval, Lawrence Berkeley Laboratory Report No. LBL-9151 (unpublished).
[59]W. Schimmerling, J. W. Kast, D. O. Dahl, R. Maidy, R. A. Cecil, B. D. Anderson, and H. R. Baldwin, Phys. Rev. Lett. 43, 1985 (1979).
[60]M. Gyulassy, private communication.
[61]R. Stock, H. H. Gutbrod, W. G. Meyer, A. M. Poskanzer, A. Sandoval, J. Gosset, Ch. King, G. King, Ch. Lukner, N. Van Sen, G. D. Westfall, and K. L. Wolf, GSI report (unpublished).